J. Fluid Mech. (1987), *vol.* 175, *pp.* 479–510
Printed in Great Britain

The effects of curvature in wall-bounded turbulent flows

By ROBERT D. MOSER AND PARVIZ MOIN†
NASA Ames Research Center, Moffett Field, CA 94035, USA

(Received 6 January 1986)

Low-Reynolds-number, mildly curved, turbulent channel flow has been simulated by direct numerical solution of the Navier–Stokes equations. Computed velocity fields were found to be in good agreement with experimental measurements. The resulting flow fields were used to study the effects of streamline curvature by comparing the concave and convex sides of the channel. Observed effects are consistent with experimental measurements for mild curvature. The most significant difference in the turbulence statistics is in the Reynolds shear stress. This is accompanied by significant differences in the terms of the equation for Reynolds-shear-stress budget. In addition, it was found that stationary Taylor–Görtler vortices were present and that they had a significant effect on the flow by contributing to the mean Reynolds shear stress, enhancing the asymmetry of the channel, and affecting the underlying turbulence.

1. Introduction

Turbulent flow over curved walls is of considerable engineering interest. However, current methods for predicting these flows are quite inadequate, as is evidenced by their performance when applied to the relatively simple curvature cases in the 1980–81 AFOSR-HTTM-Stanford Conference on Complex Turbulent Flows (Kline, Cantwell & Lilley 1982). One of the reasons for this difficulty is what Bradshaw (1973) calls 'the surprisingly large effect exerted on shear-flow turbulence by curvature of the streamlines in the plane of the mean shear'. He notes that curvature effects are often an order of magnitude greater than would be predicted by using dimensional arguments. This poor understanding of the effects of curvature greatly hinders modelling efforts.

The effects of curvature on fluid flow have been under experimental and theoretical investigation for some time. Early experimental studies of the effect of curvature on turbulence (Wilcken 1930; Wattendorf 1935) revealed changes in mean-flow properties much larger than had been predicted by mixing-length arguments. Boundary layers were observed to grow much faster on concave surfaces than on flat ones and, conversely, to grow slower on convex surfaces (Wilcken). Wall shear stresses were also greatly affected, increasing on a concave wall and decreasing on a convex wall.

Sufficiently close to the curved walls, mean-velocity profiles have been observed to obey the 'law of the wall'. This has been the case for both concave and convex curved flows in boundary layers (So & Mellor 1973, 1975; and others) and in fully developed curved-channel flow (Ellis & Joubert 1974). At larger distances from the wall, the mean velocity of a convex wall layer exceeds that of the flat-wall profile

† Also: Department of Mechanical Engineering, Stanford University, Stanford, CA 94305.

and the mean-velocity profile of a concave wall layer lies below the flat-wall profile when plotted in law-of-the-wall coordinates. The point at which these deviations occur and their magnitudes are dependent on the curvature parameter δ/R. For sufficiently weak curvature ($\delta/R \approx 0.01$), these deviations occur beyond the logarithmic region (Hunt & Joubert 1979; Hoffmann & Bradshaw 1978). It has been suggested (Hoffmann & Bradshaw 1978) that the flat-plate law of the wall applies where y/R is small (y is distance from the wall).

Turbulence quantities are also affected by curvature. In strongly curved boundary layers, the curvature effect on the turbulence intensities is very large. So & Mellor (1975) observed intensities and shear stresses of twice the flat-plate values in a concave boundary layer with $\delta/R \approx 0.1$. In a strongly curved convex boundary layer, So & Mellor (1973) and Gillis & Johnston (1983) observed that the turbulent stresses fell to zero in the outer layers. In the weakly curved boundary-layer cases ($\delta/R \approx 0.01$) of Hoffmann & Bradshaw (1978), smaller changes in turbulence quantities were observed. Changes in turbulence intensities were 10–20%, increasing on the concave wall and decreasing on the convex wall. Turbulent shear stress increased or decreased about 10% relative to the flat-wall case, with most of the change occurring in the outer layer. Even these modest changes are noteworthy since an order-of-magnitude analysis of the Reynolds-stress transport equations predicts changes an order of magnitude smaller for this mild curvature. In these investigations changes in third- and fourth-order statistics of order one were also observed.

In fully developed curved channels, similar changes in turbulence quantities have been observed (Eskinazi & Yeh 1956; Hunt & Joubert 1979). Turbulent intensities are larger on the concave side and smaller on the convex side. Also, the point where the turbulent shear stress is zero is displaced significantly toward the convex wall, and the wall shear stress is larger on the concave side than on the convex side.

A viscous stability analysis (Görtler 1940) shows that laminar flow over a concave surface is unstable at sufficiently high Reynolds number. This instability leads to a system of large longitudinal roll cells. These so-called Taylor–Görtler cells have been observed experimentally in laminar flows (Gregory & Walker 1950). Tani (1962) has suggested that there is a turbulent analogue to the laminar Taylor–Görtler vortices. He was led to this proposal after observing stationary spanwise variations in mean velocity in a concavely curved boundary layer. Similar observations have since been made by many researchers (Patel 1968; So & Mellor 1975; Meroney & Bradshaw 1975; and others). Evidence of turbulent Taylor–Görtler cells has also been found in fully developed channels (Hunt & Joubert 1979). These longitudinal vortices give rise to spanwise variations in boundary-layer thickness and skin friction. Boundary-layer thickness is greatest at the boundaries between the assumed vortices where the motion is away from the wall (outflow), and skin friction is lowest there. Turbulence quantities in the outer layer are also affected by these large longitudinal structures. In general, the effects of concave curvature on turbulence quantities are greater at the outflow boundaries between the postulated roll cells (So & Mellor 1975; Hoffmann, Muck & Bradshaw 1985).

Many researchers have observed a repeatable stationary pattern of spanwise variations. This repeatability has been attributed to upstream disturbances (Meroney & Bradshaw 1975). In an attempt to impose a more regular pattern of variations, Hoffmann *et al.* (1985) placed regularly spaced vortex generators upstream of the curved section. The resulting weak longitudinal vortices in the upstream boundary layer were amplified by the curvature, serving to 'lock in' the positions of the turbulent Taylor–Görtler cells.

Interestingly, Jeans & Johnston (1982) did not observe a stationary pattern of roll cells in their flow-visualization study on concave curvature, presumably because of a lack of persistent upstream disturbances. They observed large-scale roll-like structures (they referred to them as sweeps and ejections) which appeared randomly in time. These structures drifted in the spanwise direction and had streamwise extent as small as 'several boundary-layer thicknesses'. Barlow & Johnston (1985), using the same experimental facility, observed that the appearance of these structures was not entirely random, and that their extent and persistence were dependent on upstream conditions, for example, the condition of screens in the water channel. Barlow & Johnston (1985) also placed vortex generators upstream of the curved section and were able to make the roll-call pattern stationary, with rolls extending the entire length of the curved section.

To model the effects of curvature on the mean-flow properties, Bradshaw (1973) suggested a correction factor for the apparent mixing length in analogy to the Monin–Obouhkov formula for buoyant flows. This model has met with limited success in cases of weak curvature. More complicated schemes involving the solution of the modelled Reynolds-stress transport equations have also been used (Irwin & Smith 1975; Gibson, Jones & Younis 1981). The Reynolds-stress transport equations have additional production, convection and diffusion terms arising from the curvilinear coordinate system. These terms do not appear in scalar equations, such as those used in models based on the k–ϵ equations. In addition, it has been suggested that curvature terms, which arise naturally in the model of Launder, Reece & Rodi (1975) for the pressure–strain correlation, may account for observed curvature effects. Thus, by solving the Reynolds-stress equations, the presence of curvature is reflected in the equations being solved, rather than explicitly added to the turbulence models being used. This approach has enjoyed reasonable success.

Modelling efforts for curved flows have been hindered because the mechanism by which curvature induces the dramatic changes noted above is not well understood. The study reported here was undertaken in an attempt to improve this understanding by using numerical simulation to provide data that are not normally available from experiments. Numerical simulation of a turbulent flow can provide the turbulent velocity field as a function of space and time, which can be used to compute many quantities of interest. For example, all of the terms in the Reynolds-stress transport equation can be computed, and the contribution of the Taylor–Görtler vortices to quantities of interest can be explicitly computed.

2. The numerical simulation

To study the effects of curvature on wall-bounded turbulent flows, a simulation of curved-channel flow was performed. The three-dimensional time-dependent incompressible Navier–Stokes equations were solved in the domain bounded by sectors of concentric cylinders (see figure 1 for a scale drawing of the domain). An imposed mean-pressure gradient in the azimuthal (θ) direction drives the flow. Periodic boundary conditions are imposed in the streamwise (θ) and spanwise (z) directions, so that the flow being simulated is the fully evolved turbulent flow in a curved channel. This is a relatively difficult flow to realize in the laboratory since the flow must be allowed to develop for a long distance in the curved section. However, because it is one-dimensional in the mean, it is a particularly attractive flow for studying curvature effects and testing turbulence models.

In this simulation the Navier–Stokes equations were solved using a spectral

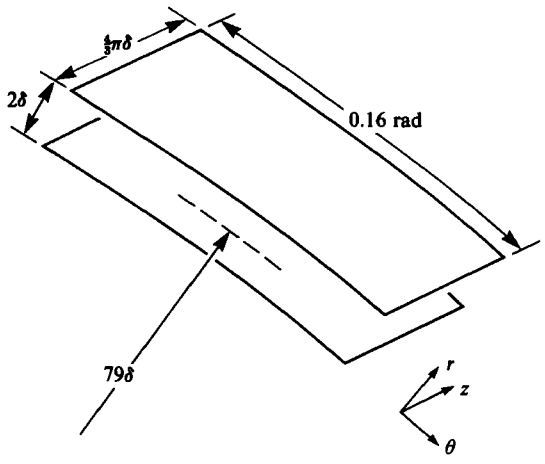

FIGURE 1. Scale drawing of the computational domain of the curved turbulent channel flow.

numerical method developed specifically for this problem (Moser, Moin & Leonard 1983). The method is based on Fourier expansions in the θ- and z-directions and Chebychev polynomial expansions in the direction normal to the walls (r). The method, and the code implementing it, were tested and verified by simulating transitions in Taylor–Couette flow; excellent agreement with theoretical, experimental and other numerical results was obtained (Moser & Moin 1984). Note that the Navier–Stokes equations were solved directly. This is in contrast to large-eddy simulations (e.g. Moin & Kim 1982), where small-scale stresses are modelled.

The curvature parameter δ/r_c, where δ is the channel half-width and r_c is the radius of curvature measured at the centreline, was chosen to be $1/79 = 0.0127$, and the Reynolds number was 2990 based on centreline mean velocity and δ. This is within the range described by Bradshaw (1973) as mild curvature ($\delta/R \approx 0.01$); Bradshaw suggested that studies on curvature effects should concentrate on mild curvature because in problems of aerodynamic interest streamline curvature is most often mild. The Reynolds number was chosen to be close to those studied by Eckelmann (1974) and Wallace, Eckelmann & Brodkey (1972). The computational domain (a scale drawing appears in figure 1) has a length of $\frac{4}{3}\pi\delta$ in the spanwise (z) direction and subtends an angle of 0.16 rad in the streamwise (θ) direction, which yields a length of 12.64δ along the centreline. These dimensions of the computational domain in the θ- and z-directions were chosen to ensure that the artificial (periodic) boundary conditions used in the θ- and z-directions do not adversely affect the computed solutions. It is necessary that the computational domain be long enough so that the computed two-point correlation functions in the θ- and z-directions fall substantially to zero in half the domain length (see Moser & Moin 1984).

Unless otherwise stated, results presented throughout this paper will be non-dimensionalized with the shear velocity and channel half-width. However, because a curved channel is not symmetric with respect to the channel centreline, the definition of the shear velocity is not unique. Three different definitions will be used. The first two are based on the wall shear stress at each of the two walls, that is,

$$U_{\tau i} = \left| \nu \frac{\partial U_\theta}{\partial r}\bigg|_{r=r_i} \right|^{\frac{1}{2}}, \quad U_{\tau o} = \left| \nu \frac{\partial U_\theta}{\partial r}\bigg|_{r=r_o} \right|^{\frac{1}{2}}. \tag{2.1}$$

These will collectively be called 'local U_τ'. The third definition is global; it is obtained by analogy with the plane channel. In the plane channel, the mean pressure gradient $\mathrm{d}\bar{P}/\mathrm{d}x$ is -1 when normalized by $\rho U_\tau^2/\delta$; in the curved channel, the mean pressure gradient is $(1/r)\,\mathrm{d}\bar{P}/\mathrm{d}\theta$ so the global U_τ is defined as

$$U_{\tau g} = \left(-\frac{1}{r_c \rho}\frac{\mathrm{d}\bar{P}}{\mathrm{d}\theta}\right)^{\frac{1}{2}} = \left(\frac{r_i^2 U_{\tau i}^2 + r_0^2 U_{\tau 0}^2}{4 r_c^2}\right)^{\frac{1}{2}}. \tag{2.2}$$

The global value $U_{\tau g}$ will be referred to simply as U_τ. All shear velocities were calculated by averaging in the z- and θ-directions as well as in time. The superscript $+$ will be used to indicate normalization by local U_τ and ν (wall coordinates). The Reynolds number based on U_τ and δ is 168 for the results presented here. This corresponds to a Reynolds number of 2990 based on the centreline mean velocity. Reynolds numbers based on $U_{\tau i}$ and $U_{\tau 0}$ (Re_i and Re_0) are 155 and 180 respectively.

In these computations, 128 Fourier modes are used to represent the velocity field in the z- and θ-directions. Chebyshev polynomials up to order 64 are used in the r-direction. In wall units, the effective grid spacing in the z-direction is $\Delta z^+ = \Delta z U_\tau/\nu = 6$, and in the θ-direction it is $r_c^+ \Delta\theta = 18$. In the r-direction, the closest effective grid point to the wall is at $y^+ = 0.2$, and towards the centre of the channel the maximum spacing is $\Delta y^+ = 8.2$. These grid spacings are representative of the resolution of the Fourier/Chebyshev velocity representation. The collocation grid used to compute the nonlinear terms has 1.5 times finer resolution in each direction to remove aliasing errors.

To evaluate the adequacy of the spatial resolution, one-dimensional energy and dissipation spectra were computed (Moser & Moin 1984). The energy spectra have at least a 100:1 reduction of the high wavenumber energy density compared with the low wavenumbers. In addition none of the energy spectra show a significant upturning at the highest wavenumbers, which would be indicative of poor resolution. Dissipation spectra have at least a 10:1 reduction at high wavenumbers compared with low wavenumbers. However, the spanwise dissipation spectra show some upturn at the high wavenumbers. The amount of dissipation in these upturned tails, which is a measure of the dissipation of the unresolved small scales, is generally less than 10% of the total dissipation. Thus most of the dissipation resides in resolved scales. These observations are evidence of the general adequacy of the computational resolution. Note that the Kolmogorov lengthscale η, which, based on average dissipation is about two wall units, is not resolved. However, most of the dissipation takes place at scales larger than 15η.

Further evidence of the adequacy of the computational resolution is the qualitative and quantitative similarity of the computed results with the experimentally observed characteristics of curved wall-bounded turbulent flows and wall-bounded turbulent flows in general. For example, the near-wall spanwise two-point correlation of u shown in figure 2(a) has a distinct negative minimum at $\Delta z^+ \approx 50$. This is clear evidence of alternating high- and low-speed regions near the wall, with mean spanwise spacing $\lambda^+ = 100$. Streamwise two-point correlation functions (Moser & Moin 1984) show that these regions are elongated in the streamwise direction. Detailed examination of instantaneous velocity fields also reveals elongated near-wall streaks with this average spacing (Moser & Moin 1984), in agreement with experimental observations (Kline *et al.* 1967). Other similarities with experimental observations will be noted throughout the following sections.

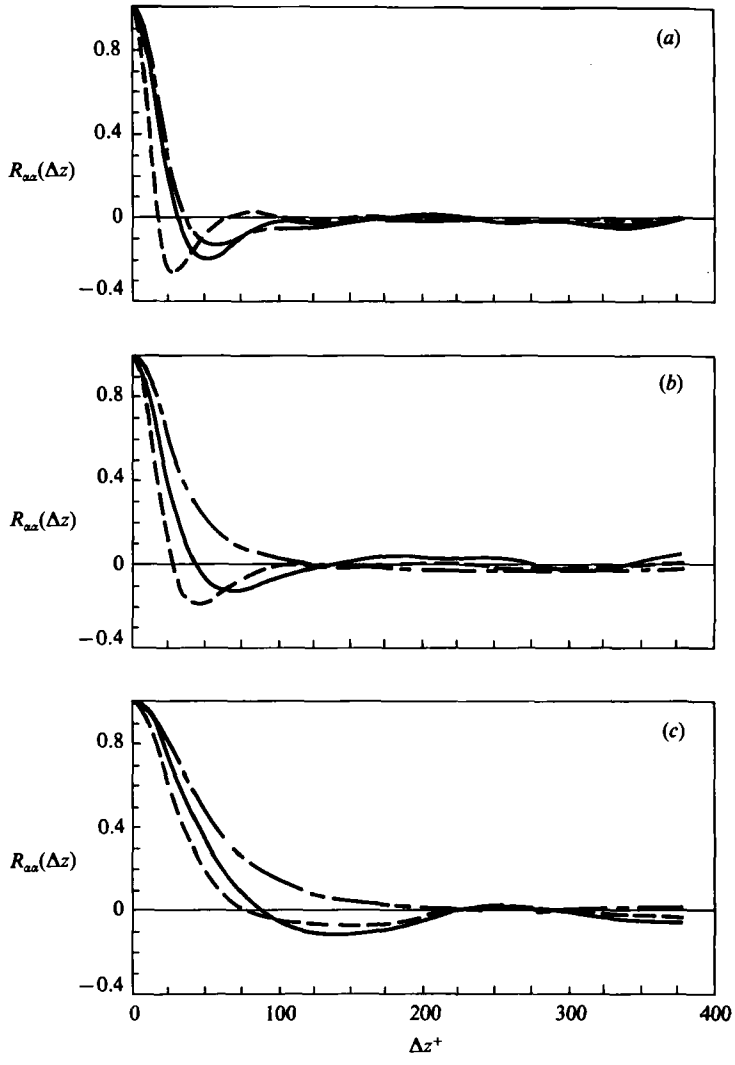

FIGURE 2. Spanwise two-point correlation functions near the concave wall: ——, $R_{\theta\theta}$; – – –, R_{rr}; – – –, R_{zz}, (*a*) $y^+ = 6.13$; (*b*) 34; (*c*) 117. Repeated indices are not summed.

In computing the convective terms, aliasing errors were removed since for time-dependent problems aliasing may be particularly damaging (Moser *et al.* 1983). A time-step of $0.0005\delta/U_\tau$ was used in these computations, which yielded a maximum Courant number of 0.8, where the Courant number C is defined as

$$C = \pi\Delta t\left(\left|\frac{v_\theta}{r\Delta\theta}\right| + \left|\frac{v_r}{\Delta r(r)}\right| + \left|\frac{v_z}{\Delta z}\right|\right).$$

The initial condition for these computations was obtained from a low-Reynolds-number, large-eddy simulation of Moin & Kim (1982). The velocity field from their calculation was simply interpolated to the collocation grid for the current calculation. It was then allowed to evolve for about $12\delta/U_\tau$, at which time the flow reached statistical equilibrium. The calculations were then continued in order to obtain an

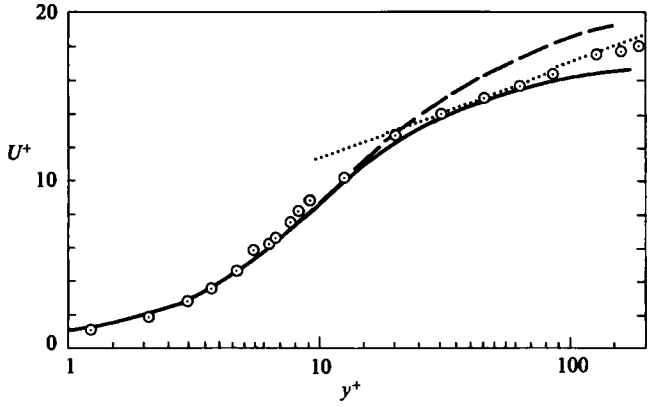

FIGURE 3. Mean velocity profile in local wall coordinates: ——, concave wall; – – –, convex wall; ⊙, plane-channel data of Wallace, Eckelmann & Brodkey (1972); ....., $U^+ = 2.5 \log y^+ + 5.5$.

adequate statistical sample. Statistics reported here were averaged over a time of about $6\delta/U_\tau$, which corresponds to $107\delta/U_{\rm cl}$, where $U_{\rm cl}$ is the centreline mean velocity. The statistics were obtained by averaging in the streamwise direction in time, and often in the spanwise direction. Space–time correlation functions of the velocity field (Moser & Moin 1984) indicate that the largest eddies are coherent for a time of about $0.5\delta/U_\tau$. Thus, the temporal averaging over $6\delta/U_\tau$ provides an approximately 12 times better sample of the largest eddies than a single velocity field. Also, the two-point spatial correlations (Moser & Moin 1984) indicate that the largest eddies are coherent in the streamwise and spanwise directions over about $\frac{1}{5}$ the computational domain in those directions. The statistics reported here therefore represent approximately 300 independent samples of the largest eddies. This statistical sample is considered marginal for some quantities (e.g. two-point correlations, spectra and high-order moments).

The computations reported here were performed on a CRAY-XMP 2/2, with a 16 megaword SSD. Computations required 22 seconds per time-step. The code for this simulation was written in VECTORAL (Wray 1983).

In the sections to follow, we shall be concerned with several types of averaging and several different velocities. To facilitate discussion, the following notation will be used. The velocity vector is denoted $\boldsymbol{v}$, with components v_r, v_θ and v_z. Two averages are defined: $\overline{a}$ is the average in θ, z and t while $\tilde{a}$ is the average in just θ and t. Several averages of the velocity are defined as $U_i = \overline{v_i}$, $u_i = v_i - U_i$, and $u_i' = v_i - \tilde{v}_i$. To facilitate comparison with the plane channel, u, v and w will be used interchangeably with u_θ, u_r and u_z; for example $U = U_\theta$ and $v' = u_r'$. All velocities are normalized by global U_τ unless otherwise indicated. When quantities are plotted in local wall coordinates, they will be normalized such that positive normal velocity is directed away from the wall.

3. Mean statistics

The mean velocity has been plotted in law-of-the-wall coordinates in figure 3. Both U^+ and y^+ are based on the local U_τ. Also plotted are the plane-channel data of Wallace *et al.* (1972) at Reynolds number $Re_\tau = 187$. Throughout this section,

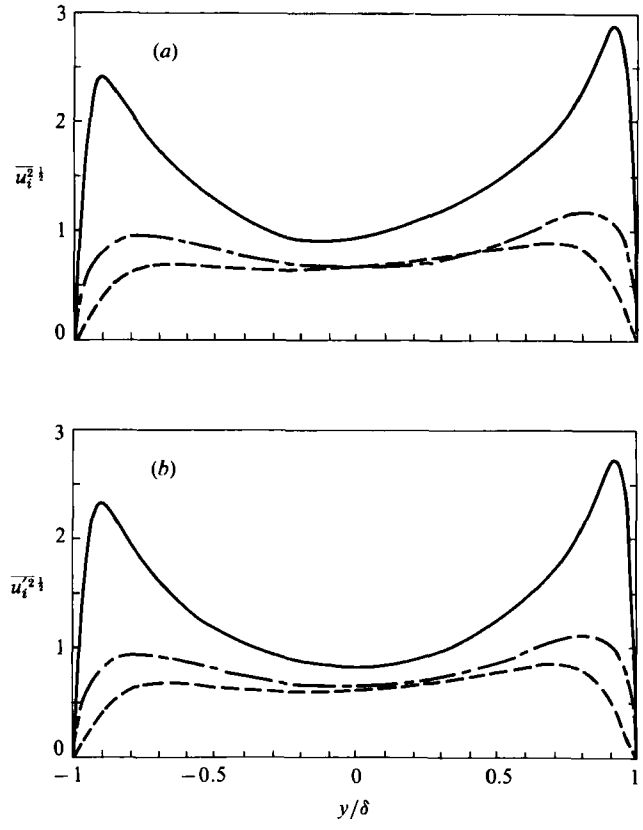

FIGURE 4. Turbulence intensities: ——, $\overline{u^{2\frac{1}{2}}}$; – – – –, $\overline{v^{2\frac{1}{2}}}$; — — —, $\overline{w^{2\frac{1}{2}}}$. (*a*) Contribution of Taylor vortices included. (*b*) Contribution of Taylor vortices excluded.

comparisons will be made with experimental data obtained in plane channels because detailed measurements of low-Reynolds-number curved channels are not available. The mean velocities on both sides of the channel and the data of Wallace *et al.* are in excellent agreement for y^+ less than 20. For y^+ greater than 20, the mean velocity of the unstable (concave) side lies below the other two. This is the experimentally observed effect of curvature. The difference between the concave- and convex-wall mean-velocity profiles is larger than can be accounted for by the small difference in local Reynolds number between the two sides. As expected the plane-channel data fall between the concave and convex profiles. Note, however, that the mean-velocity profile of Eckelmann (1974) obtained in the same facility at $Re_\tau = 146$ coincides with the convex-wall profile, which is contrary to the expected curvature effects. In the experiments of Hunt & Joubert (1979), with approximately the same curvature and a 10 times larger Reynolds number than in these computations, the mean-velocity profiles of the concave and convex sides did not diverge until $y^+ \approx 200$. In both the experiments and the computations, however, the point of divergence is at approximately the same y/r location of 0.0015 (here y is distance from the wall). This is in accordance with the conjecture of Hoffmann & Bradshaw (1978) that the location y where curvature effects on the mean velocity become significant should scale with r rather than with any shear-layer lengthscale.

Turbulent intensities as a function of radial position are shown in figure 4(*a*). As

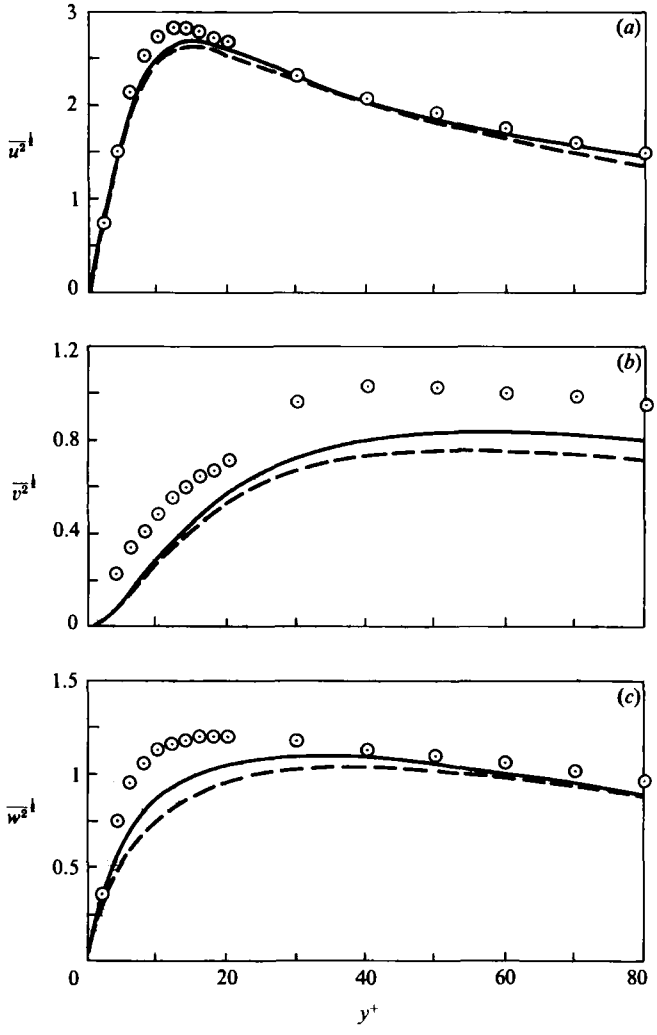

FIGURE 5. Turbulence intensities in local wall coordinates: ——, concave side; – – –, convex side; ○, plane-channel data from Kreplin & Eckelmann (1979*a*). (*a*) $\overline{u^{2\frac{1}{2}}}$; (*b*) $\overline{v^{2\frac{1}{2}}}$; (*c*) $\overline{w^{2\frac{1}{2}}}$.

expected, turbulence intensities near the concave wall are higher than those near the convex wall. As can be seen in figure 4(*b*), this difference persists even when the contribution of the Taylor–Görtler vortices $\overline{\tilde{u}_i^{2\frac{1}{2}}}$ is not included (see §4). In figure 5 the intensities $(\overline{u_i^{2\frac{1}{2}}})$ are plotted in local wall coordinates for both sides of the channel. Also plotted are the plane-channel data of Kreplin & Eckelmann (1979*a*) at Reynolds number $Re_\tau = 195$. The streamwise intensities $(\overline{u^{2\frac{1}{2}}})$ for both curved walls and the plane channel collapse when normalized in this way. The spanwise $(\overline{w^{2\frac{1}{2}}})$ and normal $(\overline{v^{2\frac{1}{2}}})$ intensities on both curved walls collapse fairly well when normalized by local U_τ. However, their agreement with the data of Kreplin & Eckelmann is not as good as that of $\overline{u^{2\frac{1}{2}}}$. In particular, the computed v-intensities are considerably below the experimental plane-channel data. Recent results of direct simulation of plane-channel flow at the same Reynolds number have a similar disagreement with the data of Kreplin & Eckelmann.

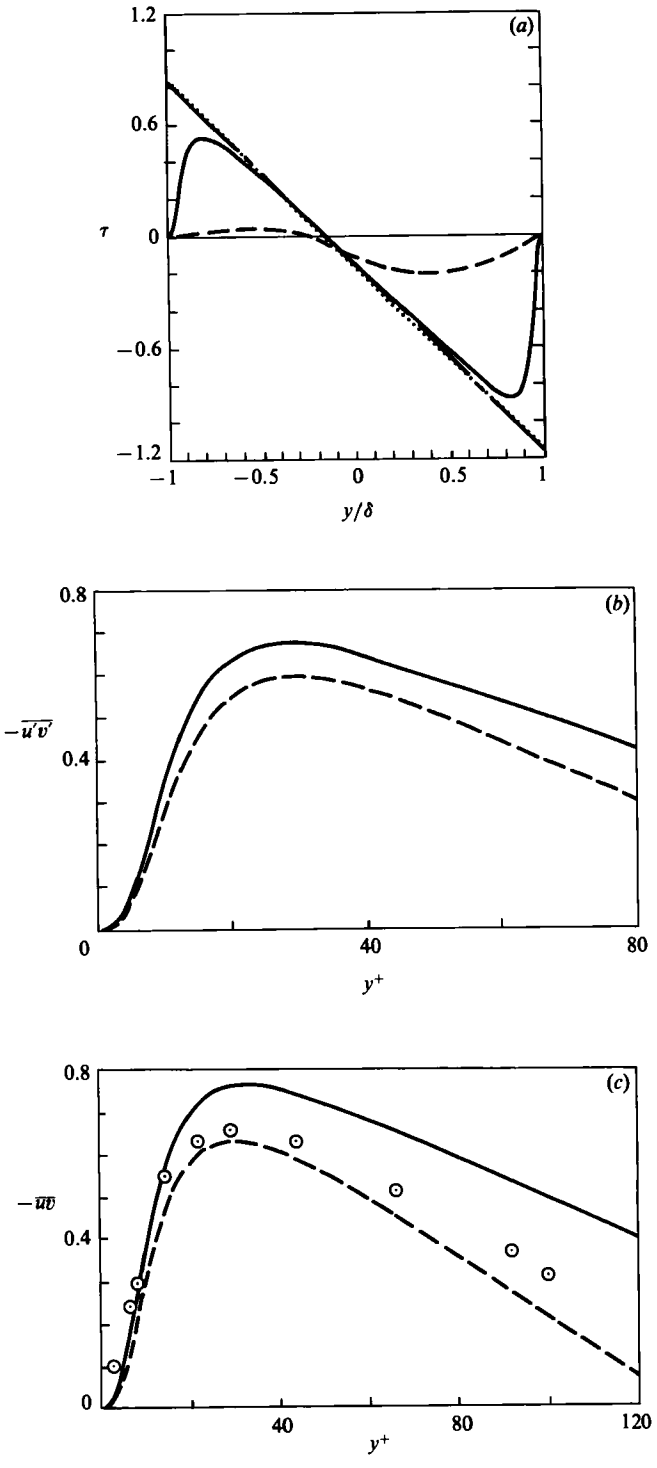

FIGURE 6. Reynolds stresses. (*a*) Global coordinates: ——, $(-\overline{uv})$; – – –, $(-\tilde{u}\tilde{v})$; — — —, viscous plus turbulent stress; ....., equilibrium stress. (*b*) $\overline{u'v'}$ in local wall coordinates: ——, concave side; – – –, convex side. (*c*) $\overline{uv}$ in local wall coordinates: ——, concave side; – – –, convex side; ○, plane-channel data from Eckelmann (1974).

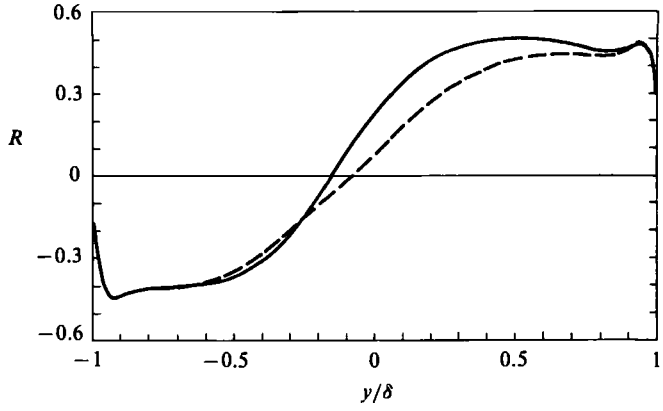

FIGURE 7. Correlation coefficient R, with and without the contribution of the Taylor–Görtler vortices. —— $(\overline{uv}/(\overline{u^2}\,\overline{v^2})^{\frac{1}{2}})$, ---- $(\overline{u'v'}/(\overline{u'^2}\,\overline{v'^2})^{\frac{1}{2}})$.

The turbulent shear stress $(-\overline{uv})$ is presented in figure 6(*a*) with the contribution of the Taylor–Görtler vortices to the turbulent stress $(-\overline{\tilde{u}\tilde{v}})$ and the total shear stress (viscous and turbulent). The differences between the concave and convex sides are striking. In particular, away from the wall the Taylor–Görtler vortices make a significant contribution to the concave-side Reynolds stress, but they contribute negligibly to the convex side. In figure 6(*b*), where $-\overline{u'v'}$ normalized by local U_τ is plotted, it is clear that the curvature has enhanced the Reynolds stress on the concave side relative to the convex side (note that there has been a sign change on the concave side to allow direct comparison of the two sides). Figure 6(*c*), in which $-\overline{uv}$ in local wall coordinates and the data of Eckelmann (1974) are plotted, shows that, except in the immediate vicinity of the wall, Eckelmann's plane-channel data at $Re_\tau = 146$ lie between the concave and convex wall Reynolds stresses. The correlation coefficient $\overline{uv}/(\overline{u^2}\,\overline{v^2})^{\frac{1}{2}}$ shown in figure 7 indicates that streamwise and normal fluctuations are better correlated on the concave side than on the convex side (coefficients of 0.5 as opposed to 0.4). Away from the wall, this is in part a result of the Taylor–Görtler vortices, as is seen in the correlation coefficient with the contribution of the vortices removed $(\overline{u'v'}/(\overline{u'^2}\,\overline{v'^2})^{\frac{1}{2}})$.

Profiles of r.m.s. vorticity fluctuations excluding the contribution of the Taylor–Görtler vortices $(\overline{\omega'^2}^{\frac{1}{2}})$ normalized by U_τ/δ are shown in figure 8(*a*). Because of the large spatial scale of the Taylor–Görtler vortices their contribution to the r.m.s. vorticity fluctuations is negligible (less than 4%). As was observed by Moin & Kim (1982), the spanwise vorticity profile attains its maximum at the wall, and falls off monotonically away from the wall, and the streamwise vorticity profile attains its maximum at the wall and has a local maximum at $y^+ \approx 20$. Note that the dissipation exhibits a similar local minimum near the wall (see §5), though no direct relationship between vorticity and dissipation is expected in this highly inhomogeneous flow. Away from the walls, the three components of the r.m.s. vorticity fluctuations are virtually identical, in contrast to the velocity fluctuations, which are significantly different. In figure 8(*b*) the r.m.s. streamwise vorticity fluctuations, non-dimensionalized by local U_τ^2/ν for each wall, are shown, as well as the plane-channel data of Kastrinakis & Eckelmann (1983), at $Re_\tau = 580$. The profiles from both walls are in very good agreement when non-dimensionalized in this way, and they are in good agreement with the plane-channel data for y^+ greater than 20. However, the

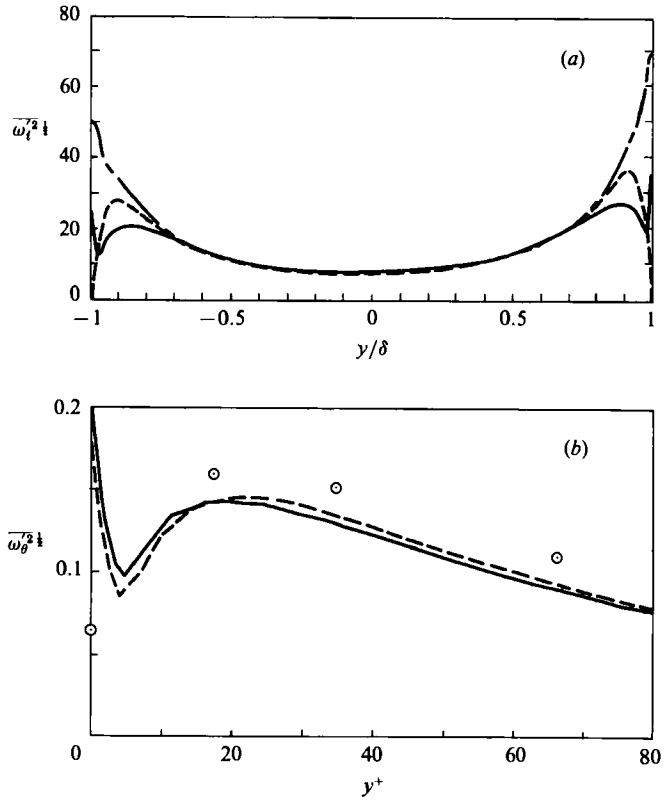

FIGURE 8. The r.m.s. vorticity fluctuations. (*a*) Global coordinates: ——, $\overline{\omega_\theta'^2}^{\frac{1}{2}}$; – – – –, $\overline{\omega_r'^2}^{\frac{1}{2}}$; – – –, $\overline{\omega_z'^2}^{\frac{1}{2}}$. (*b*) $\overline{\omega_\theta'^2}^{\frac{1}{2}}$ in local wall coordinates: ——, concave wall; – – – –, convex wall; ○, plane-channel data of Kastrinakis & Eckelmann (1983).

experimental plane-channel profile does not obtain a minimum near the wall, and the computational and experimental limiting wall values are in disagreement. Other researchers have experimentally observed a range of limiting wall values of $\overline{\omega_x'^2}^{\frac{1}{2}}$ from 0.065 to 0.12 (see Kreplin & Eckelmann 1979*a*) and Moin & Kim (1982) found a value of 0.13 in their computations; 0.19 was calculated here. The limiting wall value of the spanwise vorticity fluctuations (0.36) in the present calculations is also higher than observed experimentally (0.2 to 0.3, Kreplin & Eckelmann 1979*a*) and the computed value (0.2) of Moin & Kim (1982). The reason for this discrepancy is not known, but it is not a curvature effect since a recent direct simulation of plane-channel flow shows the same discrepancy. The plane-channel calculations of Moin & Kim (1982) and the present calculations, which use unrelated numerical methods, both show local minima in r.m.s. streamwise vorticity fluctuations near the wall. The streamwise vorticity profiles of this computation and that of Moin & Kim (1982) are consistent with the model of near-wall turbulence containing streamwise vortices. A maximum in r.m.s. vorticity away from the wall would result from the vorticity in the core of the vortices; the maximum at the wall would result from the local (spanwise) shear layer induced by the vortices as a consequence of the no-slip boundary condition on w, and the sharp minimum would occur because the streamwise vorticity in the local shear layer would be of opposite sign to that in the vortex.

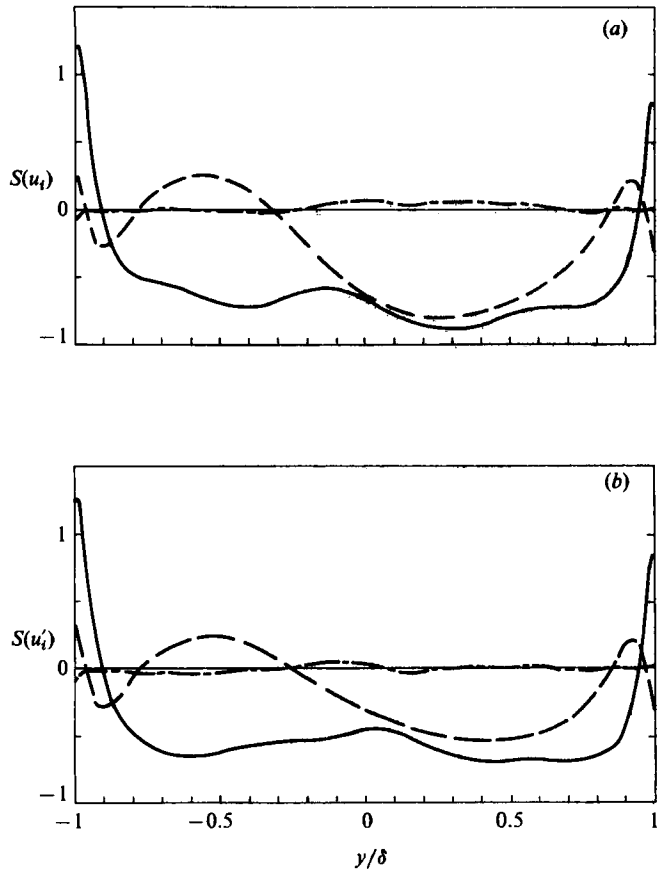

FIGURE 9. Skewness factors: ——, $S(u)$; – – –, $S(v)$; — — —, $S(w)$; (*a*) including the Taylor–Görtler contribution $S(u_t)$, (*b*) excluding the Taylor–Görtler contribution $S(u'_t)$.

In figure 9 the skewness factors of u, v and w ($S(u) = \overline{u^3}/\overline{u^2}^{\frac{3}{2}}$) are shown with and without the contribution of the Taylor–Görtler vortices; ($S(u)$ and $S(u')$). Away from the walls, the Taylor–Görtler vortices have an appreciable effect on the skewness factors. The same is true of the flatness factors. Because of the reflection symmetry of the Navier–Stokes equations, the skewness of w should be zero. The very small values of w-skewness shown in figure 9 indicate that the statistical sample from which the skewness is calculated is adequate. In figure 10, skewness factors from both sides of the channel are plotted in local y^+ coordinates, together with the data of Kreplin & Eckelmann (1979*a*) for the plane channel. Note that the u' skewness factors are in very good agreement with the plane-channel data. The agreement for the v' skewness is not nearly as good. The v' skewness of Kreplin & Eckelmann never becomes negative and has a much larger value at the wall. Also, recent $S(v)$ measurements by Alfredson & Johansson (1984), which were limited to $y^+ > 30$, show no tendency to become negative near the wall. However, negative v-skewness factors in the vicinity of the wall were also observed in the computations of Moin & Kim (1982) and the experiments of Barlow & Johnston (1985).

It is interesting that the u' skewness at the wall is approximately 60 % higher on the convex side than on the concave side, indicating that the large u-fluctuations

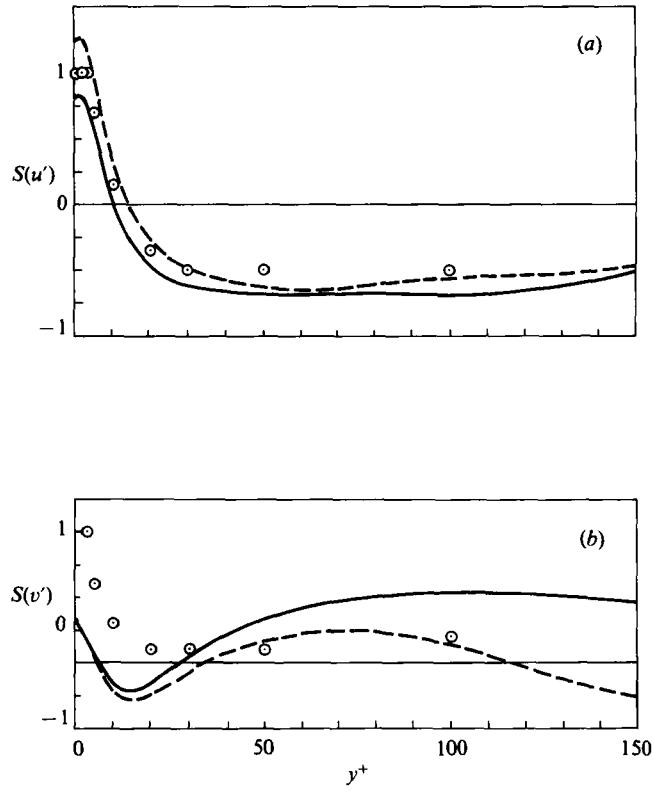

FIGURE 10. Skewness factors in local wall coordinates: ——, concave wall; – – –, convex wall; ○, plane-channel data of Kreplin & Eckelmann (1979*a*). (*a*) $S(u')$, (*b*) $S(v')$.

associated with high-speed fluid arriving from away from the wall are stronger on the convex side. This may be attributed to the effect of the Taylor–Görtler vortices on the underlying turbulence. On the concave side there is a region of strong flow away from the wall (see §4), which would tend to inhibit the motion of high-speed fluid towards the wall.

Velocity flatness factors of u', v', and w' ($F(u') = \overline{u'^4}/\overline{u'^2}^2$) are shown in figure 11. The flatness of all three velocity components are between 3 and 4 away from the walls (a Gaussian distribution has a flatness of 3). Near the wall, the flatness factors generally become large, which is indicative of intermittency or spottiness of turbulence there. The u' flatness factors for both curved walls are in good agreement with the plane-channel data of Kreplin & Eckelmann (1979*a*) (figure 12). The w' and particularly the v' flatness factors do not agree as well with the experiments. The computations of Moin & Kim (1982) show similar disagreement of v' flatness with the data of Kreplin & Eckelmann. Near the walls, the flatness of v' and w' are extremely large (30.83 for v' and 9.62 for w' at the convex wall, 27.09 and 7.57 respectively at the concave wall). Also, the flatness factors of all three velocity components are higher in the near-wall region ($y^+ < 10$) of the convex wall than near the concave wall, which suggests that the turbulence is more intermittent very near the convex wall.

In the results discussed above, it is clear that many of the curvature-induced

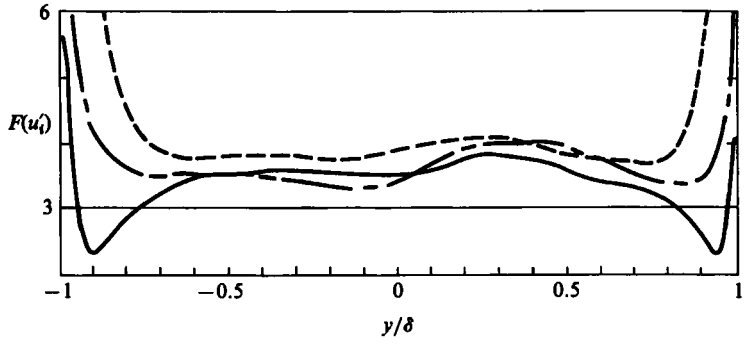

FIGURE 11. Flatness factors: ——, $F(u')$; – – – –, $F(v')$; — — —, $F(w')$.

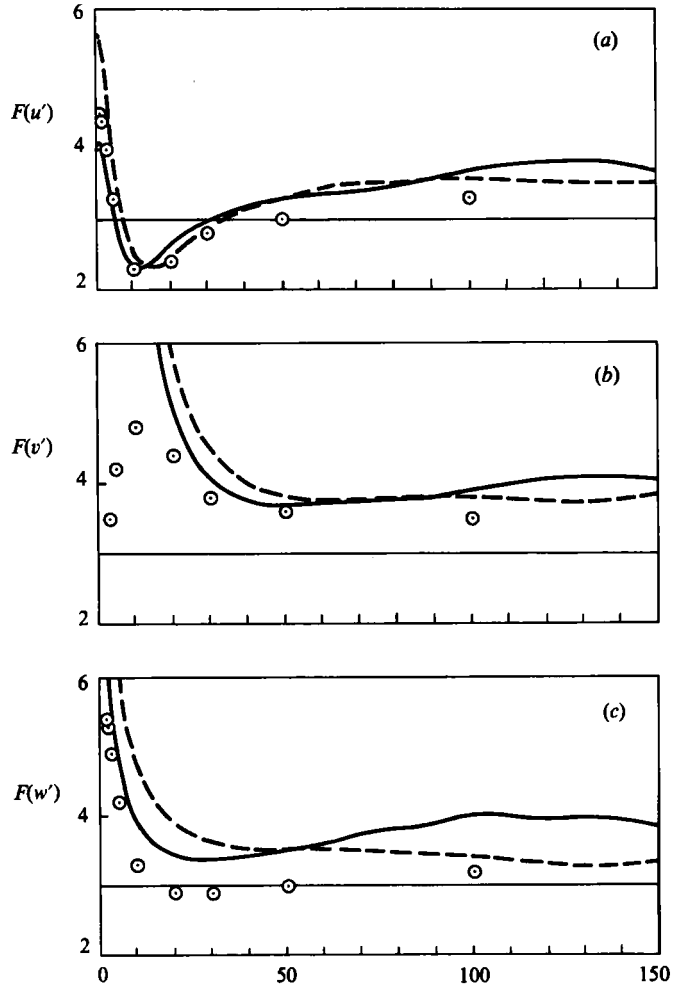

FIGURE 12. Flatness factors in local wall coordinates: ——, concave wall; – – – –, convex wall; ○, plane-channel data of Kreplin & Eckelmann (1979*a*). (*a*) $F(u')$, (*b*) $F(v')$, (*c*) $F(w')$.

	Irreducible	Taylor–Görtler	Underlying turbulence	Total
Concave wall	0.2803	0.1789	0.6899	1.1490
Convex wall	0.2851	0.0482	0.5416	0.8748

TABLE 1. Contributions to wall shear stress

differences in the turbulence statistics can be removed by scaling with the local U_τ (e.g. intensities, r.m.s. vorticity). In addition, in §5 we will see that many of the terms in the Reynolds-stress-balance equations for the concave and convex sides also collapse when scaled by local U_τ. It is therefore interesting to determine what induces the differences in wall shear stress between the convex and concave wall. By solving the mean-momentum equation, expressions can be developed for the wall shear stresses in terms of the mass flux and the turbulent shear stress:

$$\tau_{\text{wall}_\text{o}} = \frac{\partial \overline{P}}{\partial \theta}\left(\frac{1}{2} - \frac{r_\text{i}^2 \ln(r_\text{o}/r_\text{i})}{r_\text{o}^2 - r_\text{i}^2}\right) - \frac{2r_\text{i}^2/r_\text{o}\, I(r_\text{o})}{r_\text{o}^2 - r_\text{i}^2}, \tag{3.1}$$

$$\tau_{\text{wall}_\text{i}} = \frac{\partial \overline{P}}{\partial \theta}\left(\frac{1}{2} - \frac{r_\text{o}^2 \ln(r_\text{o}/r_\text{i})}{r_\text{o}^2 - r_\text{i}^2}\right) - \frac{2r_\text{o} I(r_\text{o})}{r_\text{o}^2 - r_\text{i}^2}, \tag{3.2}$$

where

$$\frac{\partial P}{\partial \theta} = \frac{8(r_\text{o}^2 - r_\text{i}^2)}{4r_\text{o}^2 r_\text{i}^2 \ln^2(r_\text{o}/r_\text{i}) - (r_\text{o}^2 - r_\text{i}^2)^2}\left(\frac{\dot{m}}{Re} + \int_{r_\text{i}}^{r_\text{o}} I(r)\,\mathrm{d}r - \tfrac{1}{2} r_\text{o} I(r_\text{o}) + \frac{r_\text{o} r_\text{i}^2 I(r_\text{o}) \ln(r_\text{o}/r_\text{i})}{r_\text{o}^2 - r_\text{i}^2}\right) \tag{3.3}$$

$$I(r) = \frac{1}{2}\int_{r_\text{i}}^{r} \left(\frac{\partial r' \overline{uv}(r')}{\partial r'} + \overline{uv}(r')\right)\left(\frac{r}{r'} - \frac{r'}{r}\right)\mathrm{d}r', \tag{3.4}$$

where $\dot{m}$ is the mass flux. Since the dependence on the turbulent shear stress $\overline{uv}$ is linear, the wall shear stress can be decomposed into a portion due to viscous stress (the shear stress due to a laminar flow at the same mass flux), a portion due to the Taylor–Görtler vortices, and a portion due to the underlying turbulence. The results of such a decomposition are shown in table 1. Note that approximately half of the difference in wall shear stress between the concave and convex walls is due to the Taylor–Görtler vortices. Thus the Taylor–Görtler vortices are very important in the establishment of the asymmetry between the concave and convex walls in the curved channel.

4. Taylor–Görtler vortices

In laboratory experiments, Taylor–Görtler vortices can be made stationary by introducing weak disturbances into the boundary layer upstream of the curved section (see § 1). These controlled disturbances have the effect of triggering the Görtler instability, causing the vortices to grow in preferred locations. In the present computation the analogous upstream disturbances are the Taylor–Görtler vortices themselves as they are convected out of the downstream end of the computational domain and are re-introduced at the upstream boundary by the periodic boundary conditions. A similar phenomenon occurs in high-Reynolds-number Taylor–Couette

flow; although the flow is fully turbulent, there are stationary, axisymmetric Taylor vortices present (Coles 1965) because of the periodicity in the azimuthal direction. Note that nothing precludes the vortices from moving in the spanwise direction; the spanwise periodicity does not force them to remain stationary. However, the periodic boundary conditions in the spanwise direction do have the effect of restricting the possible wavelengths of the Taylor–Görtler vortices. As discussed in §2, the domain width ($\frac{4}{3}\pi\delta$) was chosen to minimize the effect of the periodic boundary conditions on the turbulence. The Taylor–Görtler wavelength resulting from this choice is somewhat larger than the wavelength in the experiments of Johnston, Halleen & Lezius (1972) in a rotating channel (there is an analogy between a rotating channel and a curved channel, Bradshaw 1973). Since natural vortices which are free to form with the preferred wavelength should have maximum strength, the Taylor–Görtler vortices computed here will underestimate the strength and effects of unrestricted vortices. The results in this section concerning the effects of presumably stationary Taylor–Görtler vortices are expected to be valid for non-stationary vortices, as long as they are coherent over distances and times much larger than the length- and timescales of the underlying turbulence. Also note that these calculations are fundamentally different from the experiments in which disturbances are introduced to lock in the vortices, because here *no artificial disturbances were introduced.* The computations were started with a turbulent velocity field taken from the computations of Moin & Kim (1982) which was allowed to evolve in the curved channel. The Taylor–Görtler vortices in this computation developed from turbulent fluctuations with a broad spectrum.

In order to study turbulent Taylor–Görtler vortices they must be differentiated from the underlying turbulence. For this study the vortices are determined to be the average of the velocity field in θ and t minus the average in θ, z and t, i.e. $(\tilde{v}-\overline{v})$. Note that since the temporal average is over a finite time, the vortices that survive this averaging may actually be moving or evolving on a timescale of the averaging time ($6\delta/U_\tau$) or longer. Therefore, with the current method it is not possible to determine whether the vortices are drifting or not. If slowly drifting Taylor–Görtler vortices were present, the results of the averaging performed here would *underestimate* their strength and effects.

The Taylor–Görtler vortices were isolated by determining the average velocity $\tilde{v}$ as a function of r and z. In figure 13 the secondary-flow streamlines of the vortices are plotted. The streamlines before and after averaging over the mirror-image flow are shown. The mirror image flow $\hat{v}$ is defined by $\hat{v}_\theta(z) = v_\theta(-z)$, $\hat{v}_r(z) = v_r(-z)$, $\hat{v}_z(z) = -v_z(-z)$, where $z = 0$ is taken as the point between the two vortices. Averaging over the mirror-image flow was done because the Navier–Stokes equations are invariant to this reflection, so that the mirror-image velocity field is an equally valid solution. This procedure effectively doubles the statistical sample. Note that the effect of this averaging is to make the contour lines somewhat smoother, and to remove a minor asymmetry of the vortices. Averaging over the mirror-image flow was performed for all the remaining results in this section, which had the effect of removing similar asymmetries from the results. In this and all subsequent contour plots, negative quantities are denoted by dashed lines. The streamlines show that the vortices fill the entire channel, though they are concentrated somewhat on the concave side. Between the two vortices, where the streamlines are closely packed, is a region of relatively strong flow away from the concave wall. Flow towards the concave wall due to the Taylor–Görtler vortices is significantly more diffuse than the flow away from the concave wall.

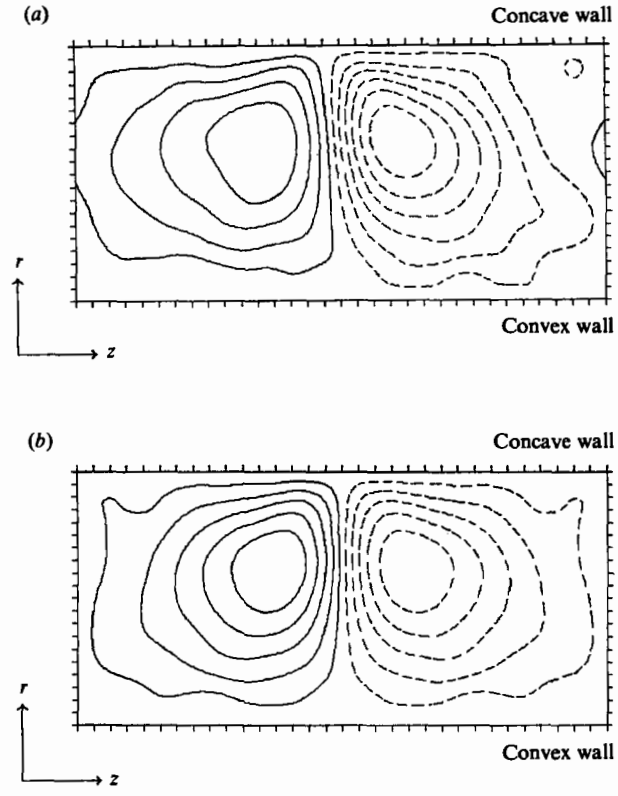

FIGURE 13. Secondary-flow streamlines of the Taylor–Görtler vortices. The top of the figure is the concave wall. (*a*) Not averaged over mirror image; (*b*) averaged over mirror image (see text). In this and subsequent contour plots, dashed contours are negative.

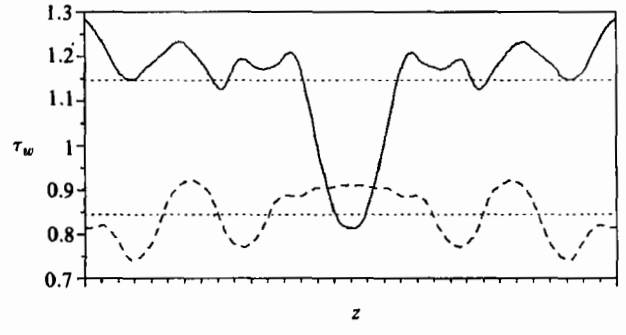

FIGURE 14. Variation of the wall shear stress in the spanwise direction: ——, concave wall; – – –, convex wall; ....., averaged values.

In figure 14 the spanwise variation of the wall shear stress is shown for both walls $((1/Re)\partial(U+\tilde{u})/\partial r|_{r=r_1,r_0})$. On the concave wall there is a very sharp minimum in shear stress located between the vortices. The oscillatory behaviour of the shear-stress curves on both walls is attributed to a poor statistical sample. On the convex side the effect of the vortices is so small that it is masked by the statistical noise.

Contours of the averaged velocities associated with the Taylor–Görtler vortices ($\tilde{u}_i$) are shown in figure 15. The intense region of negative r-velocity is evident in the area between the vortices. Note that the largest radial velocity is $0.85U_\tau$ or about 5% of the centreline mean velocity. This strong radial flow convects low-speed fluid away from the concave wall, giving rise to an area of strongly negative $\tilde{u}_\theta$ that has a magnitude as large as $2.8U_\tau$ (about 15% of the centreline velocity). It is clear that the region of strong negative $\tilde{v}$ is responsible for most of the Reynolds shear stress contributed by the Taylor–Görtler vortices, as can be seen in figure 16 where the contours of $\tilde{u}\tilde{v}$ are plotted. In the middle of the region of strong radial flow, the local Taylor–Görtler Reynolds shear stress is as high as $1.5U_\tau^2$ (recall that the maximum contribution of the vortices to total Reynolds shear stress is about $0.2U_\tau^2$). Also of interest is the significant gradient of the streamwise and spanwise Taylor–Görtler velocities ($\partial\tilde{u}/\partial r$ and $\partial\tilde{w}/\partial r$) near the concave wall, as indicated by the concentration of contour lines in figures 15(a, c). The gradient of the streamwise Taylor–Görtler velocity, which is opposite in sign to the gradient of the mean velocity, is responsible for the large defect in shear stress on the concave side (figure 14).

The Taylor–Görtler vortices affect the underlying turbulence by convecting it along the streamlines in figure 13, and by introducing a secondary strain field which contributes to its production. In figure 17 the contribution of the underlying turbulence to the components of the Reynolds-stress tensor are shown as a function of r and z. Plotted are contours of $u_i'u_j' - \overline{u_i'u_j'}$; the mean value is subtracted to make the variations more apparent. In the plots of the diagonal elements of the Reynolds-stress tensor due to underlying turbulence (figure 17a–c for $\widetilde{u_\theta'^2} - \overline{u_\theta'^2}$, $\widetilde{u_r'^2} - \overline{u_r'^2}$, and $\widetilde{u_z'^2} - \overline{u_z'^2}$ respectively) there is a strong positive region slightly away from the concave wall centred on the region of strong negative $\tilde{u}_r$ (labelled A in the figures). This is the result of convection by the Taylor–Görtler vortices and variations in production. Turbulence near the wall, where the intensities are maximum (see figure 4b), is convected towards the centre of the channel by the strong $\tilde{u}_r$. Also, in this region the magnitudes of $\partial(U+\tilde{u})/\partial r$ and $\widetilde{u_\theta' u_r'}$ are larger than the mean (see figure 15a and figure 18), so that production of $\widetilde{u_\theta'^2}$ is enhanced in this region. The positive region of $\widetilde{u_\theta'^2} - \overline{u_\theta'^2}$ is the strongest of the three, since the maximum in intensity near the wall is most pronounced for the θ-intensity, and because of the enhanced production of $\widetilde{u_\theta'^2}$. Likewise, $\widetilde{u_r'^2} - \overline{u_r'^2}$ has the weakest such positive region, because the maximum in r-intensity is least pronounced. Toward the sides of the plot domain, where $\tilde{u}_r$ is weak but positive, the opposite mechanism (fluid with a low turbulence level convected towards the concave wall by the Taylor–Görtler vortices) produces the regions of negative $\widetilde{u_i'^2} - \overline{u_i'^2}$ in the region labelled B. It could also be argued that a similar convection mechanism should be at work near the convex wall; however, the effect is much weaker and cannot be reliably differentiated from statistical noise.

Near the concave wall ($y^+ < 20$) there is a region of very intense negative $\widetilde{u_\theta'^2} - \overline{u_\theta'^2}$ under the positive regions discussed in the previous paragraph (labelled C). This is the result of depressed production in this region. Here, the magnitudes of $\partial(U+\tilde{u})/\partial r$ and $\widetilde{u_\theta' u_r'}$ are smaller than the average (figures 15a and 18) so that production of $u_\theta'^2$ is suppressed. There is a similar, though considerably weaker, negative peak in $\widetilde{u_z'^2} - \overline{u_z'^2}$ in region C, which may be a result of the depression in $\widetilde{u_\theta'^2} - \overline{u_\theta'^2}$ through interaction via the pressure–strain term. Also, near the concave wall, at either of the outer boundaries of the plotted domain, all intensities have a relatively strong positive region (especially $\widetilde{u_\theta'^2} - \overline{u_\theta'^2}$). The reason for these positive regions is not known.

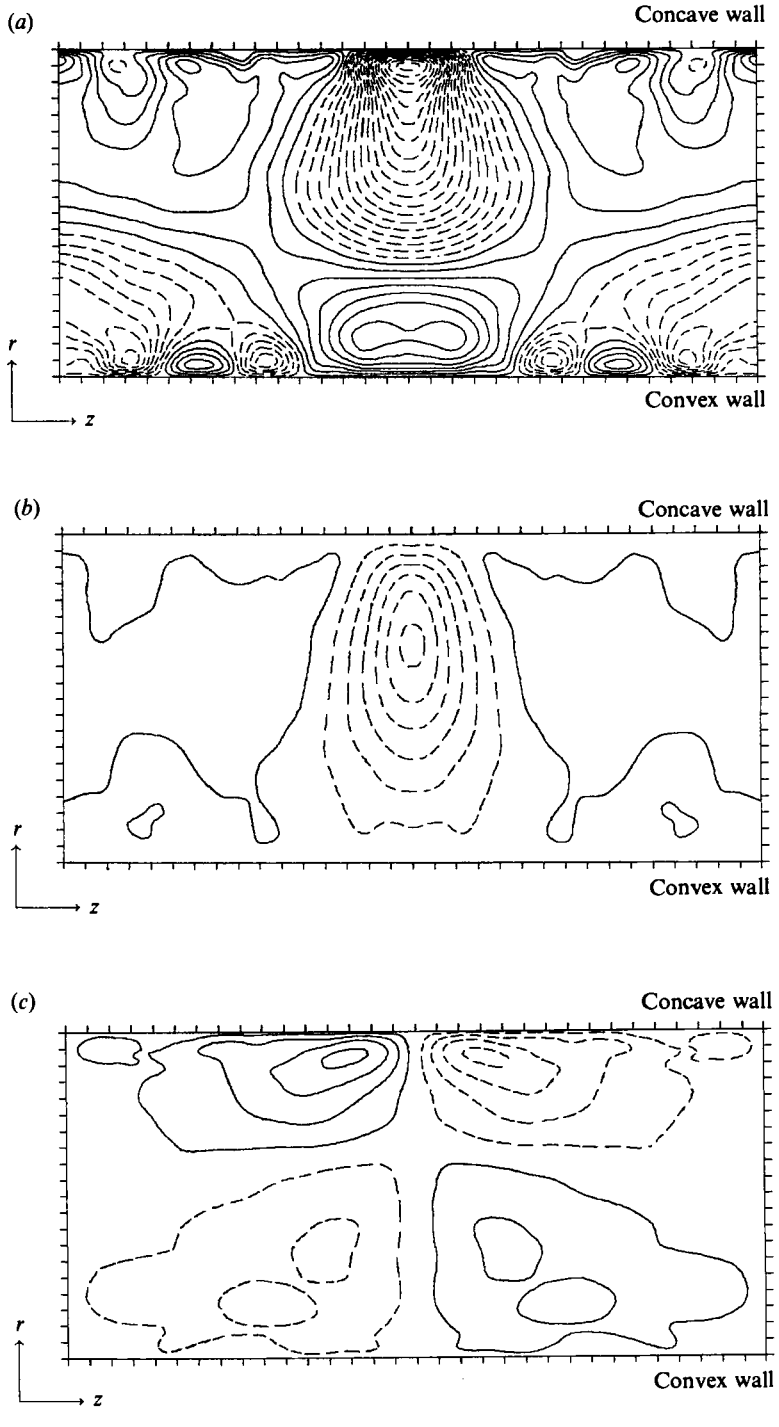

FIGURE 15. Velocities of the Taylor–Görtler vortices in the (r, z)-plane. Contours of (a) $\tilde{u}_\theta$, (b) $\tilde{u}_r$, (c) $\tilde{u}_z$. Contour levels incremented by ± 0.15, starting at ± 0.075. Dashed contours are negative.

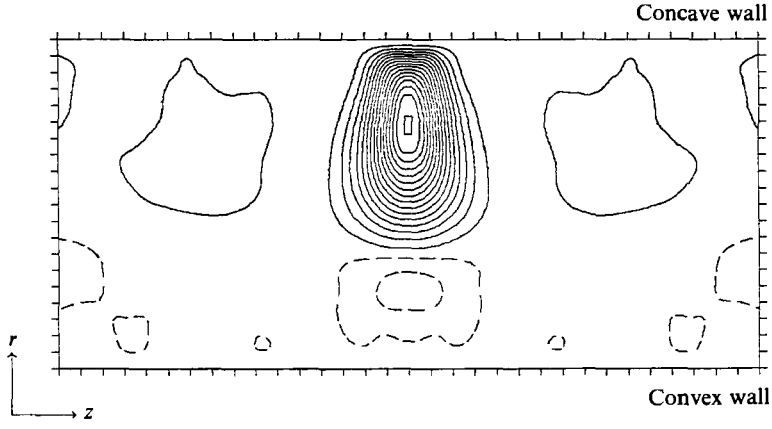

FIGURE 16. Contours of $\tilde{u}\tilde{v}$ in the (r, z)-plane. Contour levels incremented by ± 0.1, starting at ± 0.05.

The Reynolds-shear-stress term $\widetilde{u'_\theta u'_r} - \overline{u'_\theta u'_r}$ (figure 18) is similar to $\widetilde{u'^2_\theta} - \overline{u'^2_\theta}$ in that it is positive in region A and negative in regions B and C. Convection is responsible for the behaviour in regions A and B. In region C, the production of $\widetilde{u'_\theta v'_r}$ is suppressed, contributing to the negative values there.

5. Reynolds-stress budget

The Reynolds-stress equations in cylindrical coordinates are derived in Moser & Moin (1984) and elsewhere. Here we consider the Reynolds-stress equations for the special case in which the mean velocity U_θ varies only in the radial direction. For this special case, the equations are

$$\frac{\partial \overline{u^2}}{\partial t} = -2\left(\overline{uv}r\frac{\partial U/r}{\partial r} + \overline{uv}\frac{U}{r}\right) - 2\overline{uv}\frac{U}{r} - \left(\frac{1}{r}\frac{\partial r\overline{vu^2}}{\partial r} + 2\frac{\overline{vu^2}}{r}\right)$$
$$-2\overline{\frac{u}{r}\frac{\partial p}{\partial \theta}} + \frac{1}{Re}\left(\frac{1}{r}\frac{\partial}{\partial r}r\frac{\partial \overline{u^2}}{\partial r} + 2\frac{\overline{v^2}-\overline{u^2}}{r^2}\right) - \frac{2}{Re}\left(\overline{\left(\frac{\partial u}{\partial r}\right)^2} + \overline{\left(\frac{\partial u}{\partial z}\right)^2} + \frac{1}{r^2}\overline{\left(\frac{\partial u}{\partial \theta} + v\right)^2}\right); \quad (5.1a)$$

$$\frac{\partial \overline{v^2}}{\partial t} = -2\left(0 - \overline{uv}\frac{U}{r}\right) + 2\overline{uv}\frac{U}{r} - \left(\frac{1}{r}\frac{\partial r\overline{v^3}}{\partial r} - 2\frac{\overline{vu^2}}{r}\right)$$
$$-2v\overline{\frac{\partial p}{\partial r}} + \frac{1}{Re}\left(\frac{1}{r}\frac{\partial}{\partial r}r\frac{\partial \overline{v^2}}{\partial r} - 2\frac{\overline{v^2}-\overline{u^2}}{r^2}\right) - \frac{2}{Re}\left(\overline{\left(\frac{\partial v}{\partial r}\right)^2} + \overline{\left(\frac{\partial v}{\partial z}\right)^2} + \frac{1}{r^2}\overline{\left(\frac{\partial v}{\partial \theta} - u\right)^2}\right); \quad (5.1b)$$

$$\frac{\partial \overline{w^2}}{\partial t} = -0 - 0 - \frac{1}{r}\frac{\partial r\overline{vw^2}}{\partial r} - 2\overline{w\frac{\partial p}{\partial z}} + \frac{1}{Re}\left(\frac{1}{r}\frac{\partial}{\partial r}r\frac{\partial \overline{w^2}}{\partial r}\right) - \frac{2}{Re}\left(\overline{\left(\frac{\partial w}{\partial r}\right)^2} + \overline{\left(\frac{\partial w}{\partial z}\right)^2} + \frac{1}{r^2}\overline{\left(\frac{\partial w}{\partial \theta}\right)^2}\right); \quad (5.1c)$$

$$\frac{\partial \overline{uv}}{\partial t} = -\left(\overline{v^2}r\frac{\partial U/r}{\partial r} + (\overline{v^2}-\overline{u^2})\frac{U}{r}\right) - (\overline{v^2}-\overline{u^2})\frac{U}{r}$$
$$-\left(\frac{1}{r}\frac{\partial r\overline{uv^2}}{\partial r} + \left(\frac{\overline{uv^2}}{r} - \frac{\overline{u^3}}{r}\right)\right) - \left(\overline{\frac{v}{r}\frac{\partial p}{\partial \theta}} + \overline{u\frac{\partial p}{\partial r}}\right)$$
$$+\frac{1}{Re}\left(\frac{1}{r}\frac{\partial}{\partial r}r\frac{\partial \overline{uv}}{\partial r} - 4\frac{\overline{uv}}{r^2}\right) - \frac{1}{Re}\left(\overline{\frac{\partial u}{\partial r}\frac{\partial v}{\partial r}} + \overline{\frac{\partial u}{\partial z}\frac{\partial v}{\partial z}} + \frac{1}{r^2}\overline{\left(\frac{\partial u}{\partial \theta} + v\right)\left(\frac{\partial v}{\partial \theta} - u\right)}\right). \quad (5.1d)$$

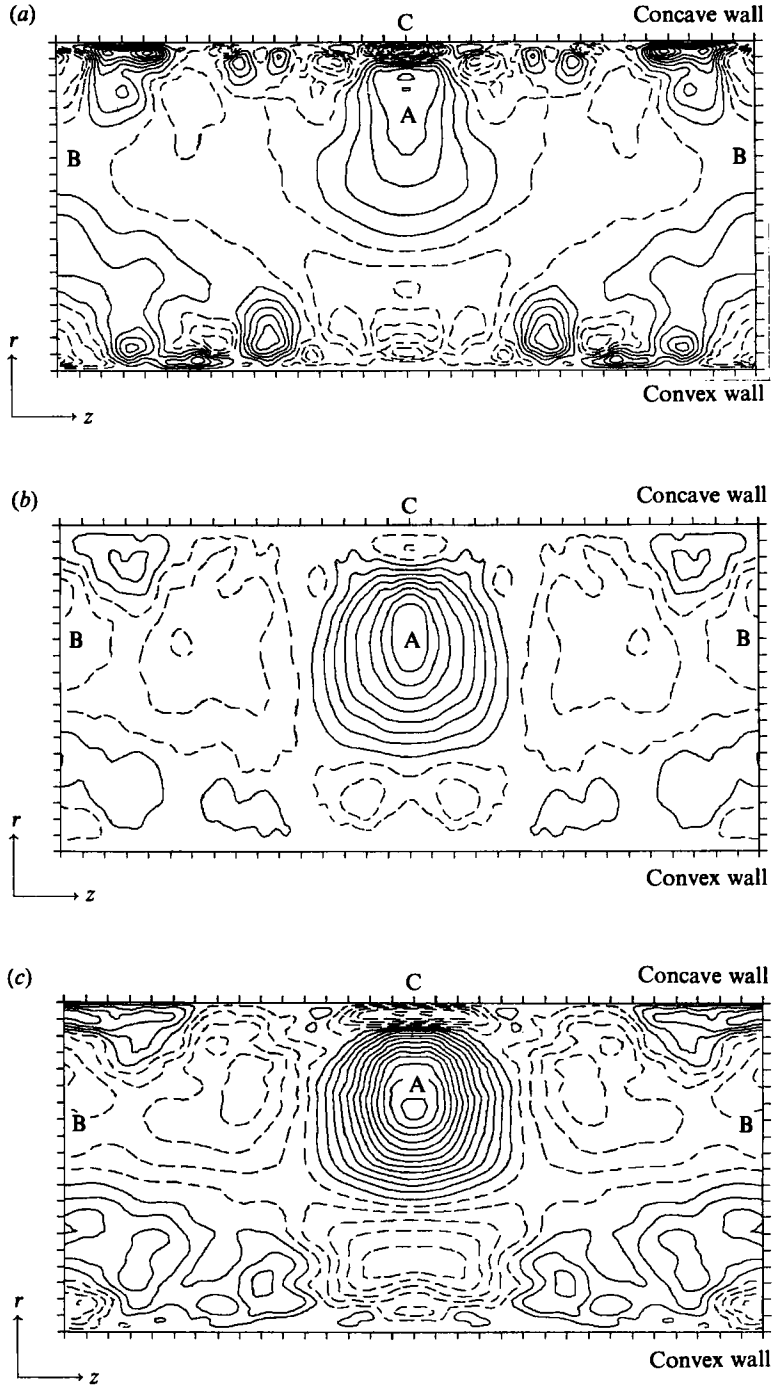

FIGURE 17. Contours of the diagonal elements of the Reynolds-stress tensor due to the underlying turbulence in the (r,z)-plane. (*a*) $\widetilde{u'^2_\theta}-\overline{u'^2_\theta}$, (*b*) $\widetilde{u'^2_r}-\overline{u'^2_r}$, (*c*) $\widetilde{u'^2_z}-\overline{u'^2_z}$. Contour levels in (*a*) are incremented by ± 0.2, starting at ± 0.1; in (*b*) and (*c*) by ± 0.05, starting at ± 0.025. Innermost negative contour in region C: (*a*) $-1.9U_\tau^2$, (*b*) $-0.08U_\tau^2$, (*c*) $-0.22U_\tau^2$.

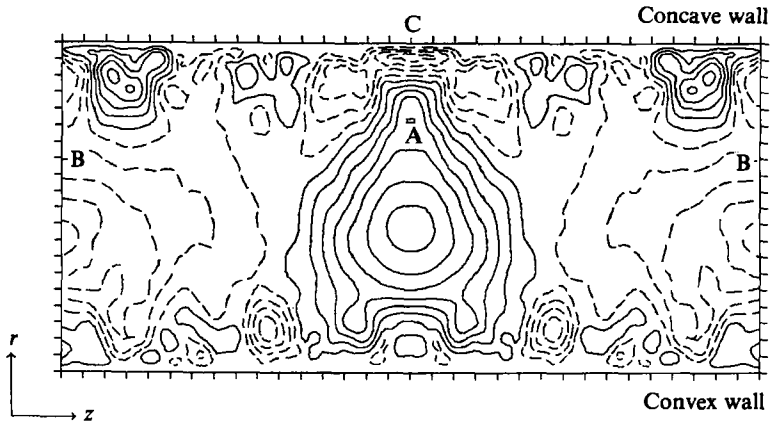

FIGURE 18. Contours of the Reynolds shear stress due to the underlying turbulence in the (r, z)-plane. Contour levels are incremented by ± 0.05, starting at ± 0.025. The innermost negative contour in region C is $-0.18U_\tau^2$.

The equation for the turbulent kinetic energy $\overline{q^2} = \frac{1}{2}(\overline{u^2}+\overline{v^2}+\overline{w^2})$ is

$$\frac{\partial \overline{q^2}}{\partial t} = -\overline{uv}r\frac{\partial U/r}{\partial r} - 0 - \frac{1}{2r}\frac{\partial r\overline{vq^2}}{\partial r} - \overline{\boldsymbol{u}\cdot\boldsymbol{\nabla}p} + \frac{1}{2Re}\left(\frac{1}{r}\frac{\partial}{\partial r}r\frac{\partial \overline{q^2}}{\partial r}\right) - \epsilon, \tag{5.2}$$

where ϵ is the dissipation of turbulent kinetic energy. In these equations the terms on the right-hand sides are labelled (in order of appearance) production, convection, turbulent diffusion, velocity–pressure gradient (VPG), viscous diffusion and dissipation. Zeros appearing in the equations indicate terms that are identically zero. Many of the terms in the Reynolds-stress equations in cylindrical coordinates do not appear in the corresponding equations in Cartesian coordinates; they are the so-called 'extra' terms (Bradshaw 1973). These terms reflect the fact that in cylindrical coordinates the orientation of the coordinate axes is a function of θ. Even though the flow is homogeneous in the θ-direction, the orientations of the mean velocity vector and the principal axes of the Reynolds-stress tensor are functions of θ. This gives rise to streamwise (θ) gradients of mean velocity and Reynolds stress.

The streamwise gradients contribute to production, convection and diffusion of the Reynolds stresses. For example, in the $\overline{u^2}$ equation the production term consists of two parts: $-2\overline{uv}r(\partial U/r)/\partial r$ which represents the production of $\overline{u^2}$ by interaction of turbulence with the mean shear; and $-2\overline{uv}(U/r)$ which is the production caused by the interaction of turbulence with the streamwise gradient of the mean-velocity vector. Similar streamwise production terms appear in the balance of $\overline{v^2}$ and $\overline{uv}$. The convection terms in each of the equations represent the convection of the Reynolds stresses by the mean velocity; this is not zero because of the streamwise gradients of the orientation of the Reynolds-stress tensor. The diffusion terms consist of diffusion in the radial direction ($(1/r)\partial r.../\partial r$) and diffusion in the streamwise direction, which acts to diminish the gradient of the stress tensor in the streamwise direction.

In the $\overline{u^2}$ equation, all the streamwise gradient terms are the same as in the $\overline{v^2}$ equation but with opposite sign, and there are no streamwise gradient terms in the $\overline{w^2}$ equation. Thus, these terms do not contribute to the equation for the kinetic

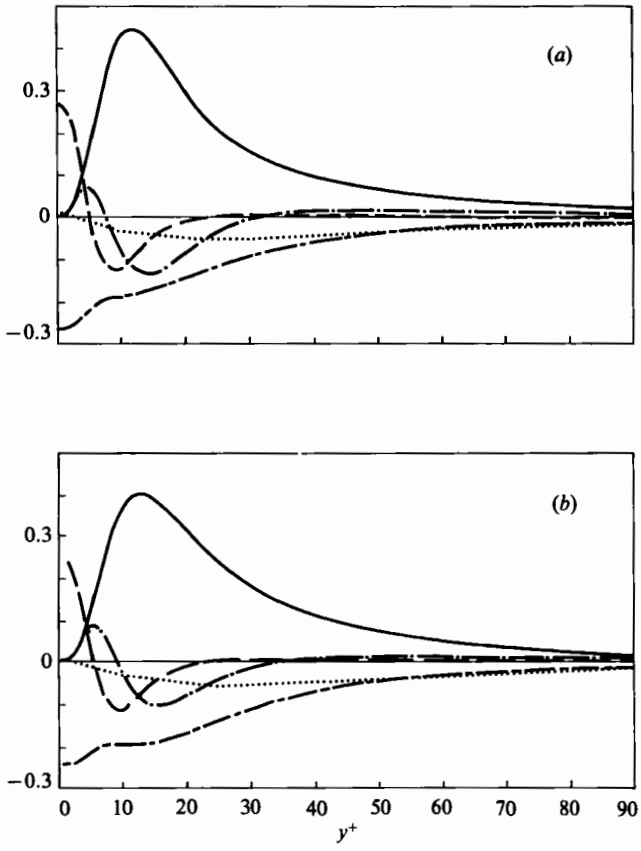

FIGURE 19. Terms in the balance of $\overline{u^{2\frac{1}{2}}}$ in local wall coordinates (terms normalized by local U_τ^4/ν): (*a*) concave wall, (*b*) convex wall. ——, production; ——, streamwise production and convection (they are equal); —·—, radial turbulent diffusion; ·····, velocity-pressure gradient; ———, dissipation; ----, radial viscous diffusion.

energy $\overline{q^2}$. The reason is that there is no streamwise gradient of $\overline{q^2}$ since it is an invariant of the Reynolds-stress tensor.

In figures 19, 20, 21 and 22 the various terms in the Reynolds-stress-balance equations (5.1) are plotted in local wall coordinates for both walls (velocities non-dimensionalized by local U_τ and lengths by ν/U_τ). This non-dimensionalization is consistent with the wall-similarity hypothesis, and attempts to eliminate the effect of the different Reynolds numbers on the concave and convex walls. Except for the streamwise convection and production (they are identical) in the $\overline{v^2}$ and $\overline{uv}$ equations, none of the terms due to streamwise gradients ('extra' terms) are included because they are negligibly small. Terms in each of the equations show remarkably little difference between the concave and convex sides of the channel when plotted in local wall coordinates. The few significant differences will be discussed after we examine the common features.

The $\overline{u^2}$ equation is largely dominated by production and dissipation. There is a large peak in production near the wall ($y^+ \approx 15$), which is balanced in part by the large dissipation near the wall. Turbulent and viscous diffusion carry $\overline{u^2}$ energy from the region of maximum production (note the minima in viscous and turbulent diffusion)

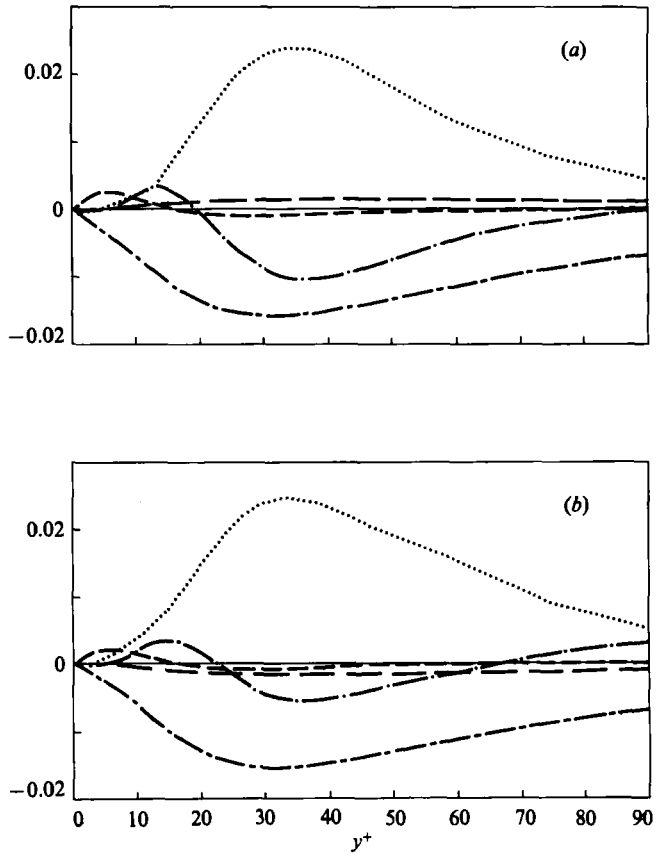

FIGURE 20. Terms in the balance of $\overline{v^2}^{\frac{1}{2}}$ in local wall coordinates: (*a*) concave wall, (*b*) convex wall. See figure 21 for symbols.

in both directions, away from and towards the wall. Very near the wall the large values of dissipation are balanced by diffusion from the maximum-production region. Far from the wall, production and the positive contribution of turbulent diffusion are balanced by dissipation and the velocity–pressure-gradient terms. In the $\overline{u^2}$ equation, the velocity–pressure-gradient term consists entirely of the pressure–strain correlation which represents transfer of energy to the other components of turbulent intensity ($\overline{v^2}$ and $\overline{w^2}$).

Since the $\overline{v^2}$ and $\overline{w^2}$ equations contain no significant production terms, their only source of energy is the pressure–strain correlation. In figure 23, the pressure–strain term appearing in the $\overline{u^2}$, $\overline{v^2}$ and $\overline{w^2}$ equations are plotted together. Beyond y^+ of 20, the major effect of the pressure–strain correlation is to distribute energy from the $\overline{u^2}$ component to the $\overline{v^2}$ and $\overline{w^2}$ components. However, close to the wall there is a large transfer from the normal component $\overline{v^2}$ to the other components. This was observed by Moin & Kim (1982) in their computations of plane-channel flow and was referred to as the 'splatting' or impingement effect. It is caused by fluid elements approaching the wall, impinging on it, and transferring their energy to motions parallel to the wall. Because of the no-slip boundary conditions and vortex stretching, the splatting effect gives rise to large streamwise and spanwise vorticity fluctuations, as seen in figure 8.

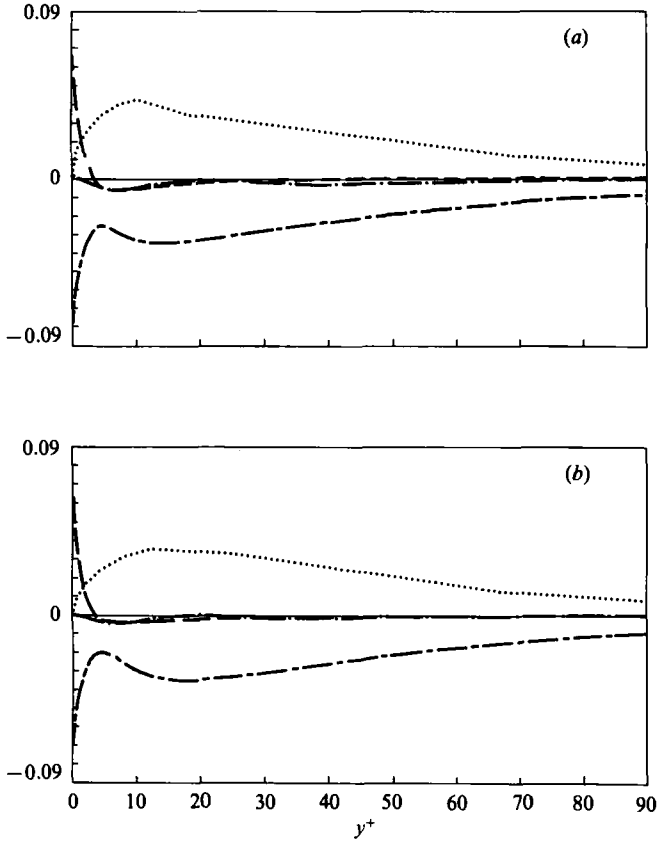

FIGURE 21. Terms in the balance of $\overline{w^2}$ in local wall coordinates: (*a*) concave wall, (*b*) convex wall. See figure 21 for symbols.

In the $\overline{v^2}$ equation, the pressure–strain and pressure-diffusion terms combine to form the velocity–pressure-gradient term. In figure 20 the velocity–pressure-gradient correlation is the major positive contribution to $\overline{v^2}$. Note that it is only slightly negative near the wall, implying that the pressure-diffusion term is positive near the wall to cancel the negative pressure–strain term. The velocity–pressure-gradient correlation, which is the source of $\overline{v^2}$ energy, is maximum at $y^+ \approx 35$. As in the $\overline{u^2}$ equation, energy is diffused from this location in both directions, toward and away from the wall, the predominant diffusive term being the turbulent diffusion. Kinematic constraints on the normal velocity ($\partial v/\partial r = 0$ at the walls) require that the viscous diffusion and viscous dissipation of $\overline{v^2}$ have zero slope at the wall. This is not apparent in figure 20; however, when the region around the origin is magnified it can be seen that these slopes are indeed zero (Moser & Moin 1984).

Pressure–strain and viscous dissipation dominate the $\overline{w^2}$ equation. Very near the wall, however, there is significant viscous diffusion.

In the $\overline{uv}$ equation, the production dominates, and again there is viscous and turbulent diffusion from the maximum source region ($y^+ \approx 15$) towards and away from the wall. However, in this case the viscous dissipation is negligible almost everywhere, and the production is balanced by the velocity–pressure-gradient and turbulent-diffusion terms.

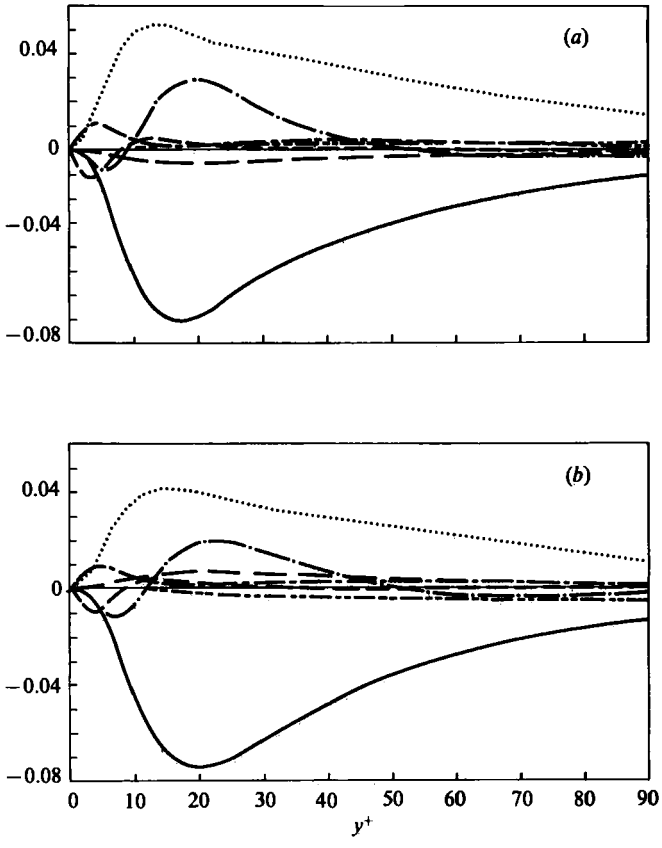

FIGURE 22. Terms in the balance of $\overline{uv}$ in local wall coordinates: (*a*) concave wall (for $-\overline{uv}$ see text), (*b*) convex wall. See figure 21 for symbols.

The current Reynolds-stress balances can be compared to those obtained by Moin & Kim (1982). As with other statistical correlations, there is a remarkable similarity between the $\overline{u^2}$ and $\overline{w^2}$ balances in this study and those reported by Moin & Kim, though there are differences in the y^+ locations of the maxima, minima and zero crossings of the various terms. In general, the y^+ location of each feature is larger in the calculations of Moin & Kim. This difference is due to inadequacies in the subgrid-scale model used in the large-eddy simulations. The $\overline{v^2}$ and $\overline{uv}$ balances appear quite different in the two calculations. However, in the case of $\overline{v^2}$, if we approach the wall from the centre of the channel, the same features are observed in both calculations though at different y^+ locations. In addition, in the vicinity of the wall ($y^+ < 15$), Moin & Kim show a relatively large magnitude of turbulent diffusion balanced by a large velocity–pressure-gradient term. This is not found in the present calculations. Note that in both calculations the location of the maximum in the turbulent diffusion term ($y^+ = 15$ here and $y^+ = 30$ in Moin & Kim) is at the same location as the minimum in the v-skewness factor. The v-skewness factor and turbulent diffusion are related because they both involve $\overline{v^3}$.

The balance of the turbulent kinetic energy $2q^2 = \overline{u^2} + \overline{v^2} + \overline{w^2}$ is shown in figure 24. The kinetic-energy equation is dominated by the $\overline{u^2}$ term, so this balance is very similar to the $\overline{u^2}$ balance. As was seen above, the turbulent diffusion is positive very

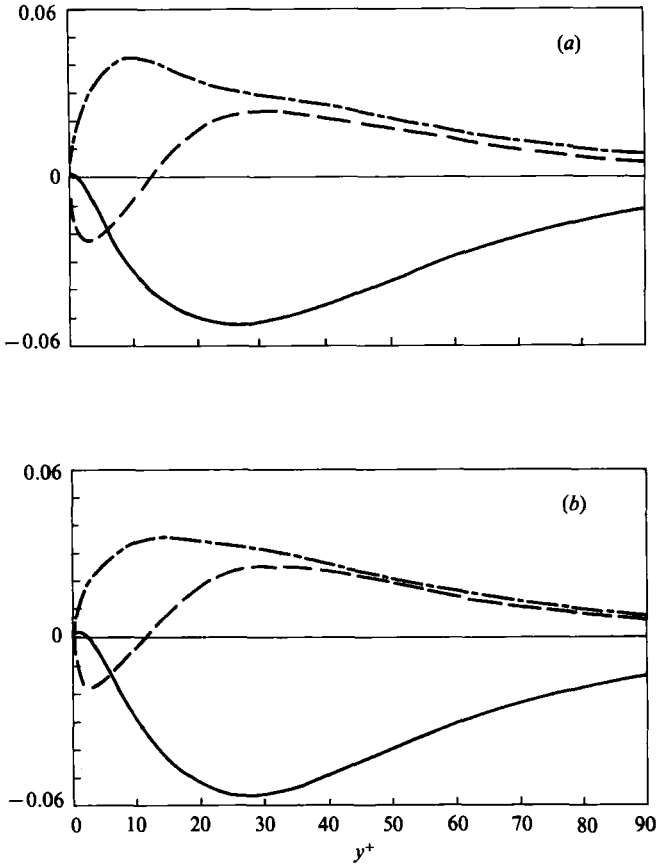

FIGURE 23. Diagonal elements of the pressure–strain correlation tensor Φ: ——, $\Phi_{\theta\theta}$; – – – –, Φ_{rr}; — — —, Φ_{zz}. (*a*) concave side, (*b*) convex side.

near the wall as a result of the diffusion of energy from the maximum source region. In contrast, the estimated balance of Townsend (1976) shows no positive region of turbulent diffusion. Moreover, Townsend shows a very large pressure-diffusion term near the wall which is also contrary (in relative magnitude) to the current results and to those of Moin & Kim (1982). Townsend's estimates for the remaining terms are in qualitative agreement with the current calculations.

As was noted above, the terms of the Reynolds-stress balance are remarkably similar on the convex and concave sides (when normalized by local wall variables). There are, however, several notable differences. In the $\overline{u^2}$ equation, the production is somewhat higher on the concave side (about 10%), and near the wall ($y^+ < 25$) the turbulent diffusion is lower. The same is true in the $\overline{v^2}$ balance. Also, in the $\overline{v^2}$ equation, streamwise production and convection (they are identical) make a small positive contribution on the concave side and a small negative contribution on the convex side. Note that the same terms appear with opposite sign in the $\overline{u^2}$ equation, but in that equation other terms are much larger. The $\overline{uv}$ balances show the most differences between the concave and convex sides. This is not surprising since $\overline{uv}$ itself shows more differences between the two sides than the turbulence intensities. On the concave side the peak production of $-\overline{uv}$ is about 5% less than on the convex side, a result of the smaller values of $\partial U/\partial r$ on the concave side when expressed in local

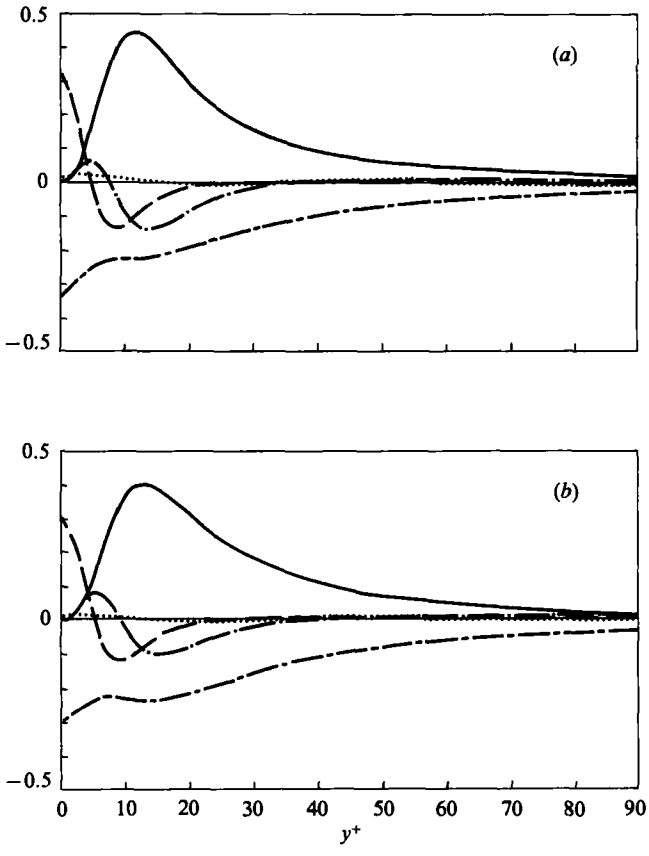

FIGURE 24. Terms in the balance of $2q^2 = \overline{u^2}+\overline{v^2}+\overline{w^2}$ in local wall coordinates: (*a*) concave wall, (*b*) convex wall. See figure 21 for symbols.

wall coordinates. The velocity–pressure-gradient term is as much as 20% greater on the concave side, and the turbulent diffusion from the maximum source region is about 40% higher on the concave side. In this balance streamwise convection and production are not negligible, they contribute to $-\overline{uv}$ on the concave side and diminish $-\overline{uv}$ on the convex side. Streamwise convection and production are strongest near the walls ($y^+ \approx 15$), where they contribute about 10% of production, and slowly decrease towards the centre of the channel.

It is interesting to consider the sign with which the streamwise gradient ('extra') terms contribute to the Reynolds-stress budgets on the two sides of the channel. It was noted above that the streamwise convection terms contributed with opposite sign on the two sides. All the other 'extra' terms except the streamwise viscous diffusion also contribute with opposite sign on the two sides of the channel. These terms have not been plotted because they are negligibly small; however, their behaviour with respect to sign on the two sides of the channel can be deduced from the following argument. Assuming that the behaviour of statistical quantities on the concave and convex walls is similar (as has been observed), it can be seen that, for a particular term in (5.1), if the sum of the exponent on vertical velocity v in the term and the number of vertical (r) derivatives is even (odd for the $\overline{uv}$ equation) then that term will contribute with the same sign on the two sides of the channel. Otherwise it will

contribute with opposite sign. All normal terms necessarily contribute with the same sign on the two sides of the channel. Note that the streamwise viscous diffusion and streamwise turbulent diffusion are different in this regard; that is, streamwise turbulent diffusion contributes with opposite sign on the two sides while streamwise viscous diffusion does not. Viscous diffusion is by definition driven by Reynolds-stress gradients, thus the model of streamwise turbulent diffusion being driven by Reynolds-stress gradients is particularly inappropriate. In fact, unlike the normal turbulent diffusion, the streamwise turbulent diffusion transports Reynolds stress against the prevailing streamwise gradient of Reynolds stress in most of the convex side of the channel ($y^+ > 10$). This observation is of little consequence for the current mild-curvature case, since the streamwise turbulent diffusion is negligible in all the Reynolds-stress balances. However, it is expected that in strong curvature this term will be important.

Many of the differences cited above are in the turbulent-diffusion and pressure–strain terms. The turbulent-diffusion terms in these calculations include several effects: the convection of the underlying turbulence by the Taylor–Görtler vortices, the actual turbulent diffusion of the underlying turbulence and the enhancement (or diminishment) of that diffusion by the centrifugal instability mechanism. The effects of the Taylor–Görtler vortices and the centrifugal mechanism on the concave walls will be opposite to that on the convex wall, so it is not surprising that the turbulent diffusion is different on the two walls. This is in accordance with Bradshaw's (1973) assertion that curvature effects on the Reynolds-stress equations must appear in the higher-order statistical correlations. Bradshaw's argument would also suggest that the pressure–strain terms should be affected since they can be expressed as integrals of two-point triple correlations of the velocity gradients (see for example Launder *et al.* 1975). The significant curvature effects on the $\overline{uv}$ pressure–strain terms is also in accordance with the suggestions of Launder *et al.* and So (1975) that curvature effects can be accounted for by properly modelling the pressure–strain terms.

Note that the dissipation terms, which are dominated by the small scales, are in very good agreement on the two walls. Also, as noted in §5.1, the r.m.s. vorticity fluctuations, which are sensitive to the small scales, were in good agreement in local wall variables. This suggests that curvature has a minimal effect on the small scales of turbulence.

6. Conclusions

A direct numerical simulation of a low-Reynolds-number, fully developed curved turbulent channel flow has been performed. Simulation results exhibit remarkable qualitative and quantitative agreement with the experimental observations, and have all the features of a wall-bounded turbulent flow, including near-wall streaks with the experimentally observed mean spacing.

The results of this simulation have been examined for curvature effects and their causes; the following specific observations were made.

(i) Many of the turbulence statistics of interest are the same on the concave and convex sides of the channel when scaled in local wall variables.

(ii) The most significant exceptions to the similarity of the concave and convex walls in local wall variables are the Reynolds shear stress and the terms of the equation for the Reynolds-shear-stress balance. Near-wall skewness and flatness factors were also affected.

(iii) Taylor–Görtler vortices are directly responsible for approximately half of the

difference in Reynolds shear stress between the two sides of the channel in local wall variables. They are also responsible for half of the difference between the wall shear stresses.

(iv) Differences in the equations for the Reynolds-shear-stress balance between the two walls are most prominent in the turbulent-diffusion and velocity–pressure-gradient terms.

(v) In the $\overline{v^2}$ balance equation and the equation for the Reynolds-shear-stress balance, streamwise ('extra') production and convection are not negligible. These terms contribute with opposite signs on the concave and convex walls, enhancing differences between the two sides.

(vi) Streamwise turbulent diffusion and streamwise viscous diffusion have qualitatively different behaviour. Streamwise turbulent-diffusion transport is against the streamwise Reynolds-stress gradients on the convex side. This is expected to be important in strong curvature cases.

These observations suggest some possible explanations for the difficulties that have been experienced in modelling curved flows, especially concave curved flows. First, the modelled computations are usually two-dimensional (streamwise and normal) and do not explicitly account for the presence of Taylor–Görtler vortices which are shown here to have a significant impact on the turbulence statistics. Terms in the turbulent kinetic-energy equation (as well as many other quantities) are relatively insensitive to the presence of the curvature (when normalized in wall variables), so that a standard k–ϵ model is not likely to produce significant curvature effects. The important differences in the shear-stress equation due to curvature appear in terms which must be modelled in a Reynolds-stress formulation. In cases of strong curvature the streamwise turbulent-diffusion term is expected to be important; however, this term is inconsistent with gradient-diffusion models.

This work is based in part on the doctoral dissertation of R. D. Moser at Stanford University. The authors gratefully acknowledge useful discussions with Professors A. Leonard, W. C. Reynolds and J. H. Ferziger. Dr J. Kim made numerous helpful comments on a draft of this paper.

REFERENCES

ALFREDSON, P. H. & JOHANSSON, A. V. 1984 On the detection of turbulence-generating events. *J. Fluid Mech.* **139**, 325.

BARLOW, R. S. & JOHNSTON, J. P. 1985 Structure of turbulent boundary layers on a concave surface. *Rep. MD-47*, Department Mechanical Engineering, Stanford Univ., Stanford, California.

BRADSHAW, P. 1973 The effects of streamline curvature on turbulent flow. *AGARDograph* no. 169.

COLES, D. 1965 Transition in circular Couette flow. *J. Fluid Mech.* **21**, 385.

ECKELMANN, H. 1974 The structure of the viscous sublayer and the adjacent wall region in a turbulent channel flow. *J. Fluid Mech.* **65**, 439.

ELLIS, L. B. & JOUBERT, P. N. 1974 Turbulent shear flow in a curved duct. *J. Fluid Mech.* **62**, 65.

ESKINAZI, S. & YEH, H. 1956 An investigation on fully developed turbulent flows in a curved channel. *J. Aero. Sci.* **23**, 23.

GIBSON, M. M., JONES, W. P. & YOUNIS, B. A. 1981 Calculation of turbulent boundary layers on curved surfaces. *Phys. Fluids* **24**, 386.

GILLIS, J. C. & JOHNSTON, J. P. 1983 Turbulent boundary-layer flow and structure on a convex wall and its redevelopment on a flat wall. *J. Fluid Mech.* **135**, 123.

GÖRTLER, H. 1940 On the three dimensional instability of laminar boundary layers on concave walls. *NACA TM-137.*

GREGORY, N. & WALKER, W. S. 1950 The effect of isolated surface excrescences in the boundary layer. *Aero. Res. Counc. R&M* 2779.

HOFFMANN, P. H. & BRADSHAW, P. 1978 Turbulent boundary layers on surfaces of mild longitudinal curvature. *Imperial College Aeronautics Rep.* 78-04.

HOFFMANN, P. H., MUCK, K. C. & BRADSHAW, P. 1985 The effect of concave surface curvature on turbulent boundary layers. *J. Fluid Mech.* **161**, 371–403.

HUNT, I. A. & JOUBERT, P. N. 1979 Effects of small streamline curvature on turbulent duct flow. *J. Fluid Mech.* **91**, 633.

IRWIN, H. P. A. H. & SMITH, P. A. 1975 Prediction of the effect of streamline curvature on turbulence. *Phys. Fluids* **18**, 624.

JEANS, A. H. & JOHNSTON, J. P. 1982 The effect of streamwise concave curvature on turbulent boundary layer structure. *Rep. MD-40*, Department Mechanical Engineering, Stanford Univ., Stanford, California.

JOHNSTON, J. P., HALLEEN, R. M. & LEZIUS, D. K. 1972 Effects of spanwise rotation on the structure of two-dimensional fully developed channel flow. *J. Fluid Mech.* **56**, 533.

KASTRINAKIS, E. G. & ECKELMANN, H. 1983 Measurement of streamwise vorticity fluctuations in a turbulent channel flow. *J. Fluid Mech.* **137**, 165.

KLINE, S. J., CANTWELL, B. J. & LILLEY, G. M. (eds) 1982 *Proc. 1980–81 AFOSR-HTTM-Stanford Conference on Complex Turbulent Flows*, vol. 1. Department Mechanical Engineering, Stanford Univ., Stanford, California.

KLINE, S. J., REYNOLDS, W. C., SCHRAUB, F. A. & RUNSTADLER, P. W. 1967 The structure of turbulent boundary layers. *J. Fluid Mech.* **30**, 741.

KREPLIN, H. & ECKELMANN, H. 1979*a* Behavior of the three fluctuating velocity components in the wall region of a turbulent channel flow. *Phys. Fluids* **22**, 1233.

KREPLIN, H. & ECKELMANN, H. 1979*b* Propagation of perturbations in the viscous sublayer and adjacent wall regions. *J. Fluid Mech.* **95**, 305.

LAUNDER, B. E., REECE, G. J. & RODI, W. 1975 Progress in the development of a Reynolds-stress turbulence closure. *J. Fluid Mech.* **68**, 537.

MERONEY, R. N. & BRADSHAW, P. 1975 Turbulent boundary-layer growth over a longitudinally curved surface. *AIAA J.* **13**, 1448.

MOIN, P. & KIM, J. 1982 Numerical investigation of turbulent channel flow. *J. Fluid Mech.* **118**, 341.

MOSER, R. D. & MOIN, P. 1984 Direct numerical simulation of curved turbulent channel flow. *NASA TM-85974.*

MOSER, R. D., MOIN, P. & LEONARD, A. 1983 A spectral numerical method for the Navier–Stokes equations with applications to Taylor–Couette flow. *J. Comp. Phys.* **52**, 524.

PATEL, V. C. 1968 Measurements of secondary flow in the boundary layers of a 180° channel. *ARC Rep. 30428.*

SO, R. M. C. 1975 A turbulent velocity scale for curved shear flows. *J. Fluid Mech.* **70**, 37.

SO, R. M. C. & MELLOR, G. L. 1973 Experiment on convex curvature effects in turbulent boundary layers. *J. Fluid Mech.* **60**, 43.

SO, R. M. C. & MELLOR, G. L. 1975 Experiment on turbulent boundary layers on a concave wall. *Aero. Quart.* **26**, 35.

TANI, I. 1962 Production of longitudinal vortices in the boundary layer along a concave wall. *J. Geophys. Res.* **67**, 3075.

TOWNSEND, A. A. 1976 *The Structure of Turbulent Shear Flow*, p. 145. Cambridge University Press.

WALLACE, J. M., ECKELMANN, H. & BRODKEY, R. S. 1972 The wall region in turbulent shear flow. *J. Fluid Mech.* **54**, 39.

WATTENDORF, F. L. 1935 A study of the effect of curvature on fully developed turbulent flow. *Proc. R. Soc. Lond.* **148**, 565.

WILCKEN, H. 1930 Effect of curved surfaces on turbulent boundary layers. *NASA TT-F-11,421.*

WRAY, A. A. 1983 *VECTORAL for FORTRAN users.* (Available from the author.) NASA Ames Research Center, Moffett Field, California.